nature communications

Article

https://doi.org/10.1038/s41467-026-69899-8

Eukaryote initiation factor 6 modulates small-cell lung carcinoma plasticity via the integrin-FAK signaling axis

Received: 4 May 2025

Accepted: 11 February 2026

Published online: 24 February 2026

Check for updates

Haoning Peng[1,2,3,8], Zhile Wang[1,2,8], Mengyao Wang[1,8], Zheyu Ding[1], Kaixiu Li[1], Yuqing Wang[1], Xuejiao Yu[4], Siyang Song[4], Yulan Deng[1], Yi Liu[1,2], Qiang Pu[1,2], Lu Li[5], Michael Cerezo[6,7], Weiya Wang[4], Lunxu Liu[1,2] ✉ & Shensi Shen[1,2] ✉

Small cell lung carcinoma (SCLC) is an aggressive neuroendocrine cancer that rapidly develops resistance to platinum-based chemotherapy. A key feature of SCLC is its ability to switch between neuroendocrine (NE) and non-neuroendocrine (non-NE) states, a process linked to therapeutic failure, yet the underlying mechanisms driving this plasticity remain incompletely understood. Here, we show that the translation initiation factor eIF6 is a critical regulator of non-NE transdifferentiation in SCLC. eIF6 expression is consistently upregulated in non-NE states across cell lines, mouse models, and patient samples, accompanied by global remodelling of the translational landscape. Mechanistically, eIF6 dissociates from ribosomes and interacts with the CD104-FAK complex, leading to MAPK pathway activation. Intervening eIF6 suppresses non-NE transdifferentiation and enhances SCLC chemotherapy sensitivity in vitro and in vivo. These findings position the eIF6-CD104-FAK axis as a prognostic marker and therapeutic target, offering a potential strategy to mitigate SCLC resistance.

Small cell lung carcinoma (SCLC), a high-grade neuroendocrine (NE) cancer that accounts for ~15% of all lung cancers[1]. SCLC is characterized by a high mutation burden, primarily driven by its strong association with tobacco exposure and frequent loss-of-function alterations in RB1 (~74%) and TP53 (~92%). Its recalcitrant nature is evident in the rapid disease progression and early metastasis, with over two-thirds of patients presenting with advanced-stage disease at the time of diagnosis[2]. For more than three decades, platinum-based combination chemotherapy has been the standard front-line treatment for SCLC. More recently, the addition of immune checkpoint blockade has extended the therapeutic options. Combining platinum-based chemotherapy with anti-PD-L1 immunotherapy, such as durvalumab or atezolizumab, has shown improved overall survival by ~3 months in patients with extensive-stage SCLC (ES-SCLC)[3,4]. Despite an initial treatment response rate of 60-80%, relapse (~90%) is common and rapid, with median survival for ES-SCLC patients remaining below 10 months, highlighting the urgent need for strategies to achieve durable clinical outcomes.

Tumour cell plasticity, an emerging hallmark of cancer, drives cell state diversity and contributes to therapy resistance[5]. Once viewed as a homogeneous disease, SCLC is now recognized as a highly heterogeneous and plastic tumour comprising distinct molecular subtypes:

[1]Institute of Thoracic Oncology, Frontiers Science Center for Disease-related Molecular Network, National Clinical Research Center for Geriatrics, West China Hospital, Sichuan University, Chengdu, China. [2]Department of Thoracic Surgery, West China Hospital, Sichuan University, Chengdu, China. [3]Department of Thoracic Surgery, Zhongshan Hospital, Fudan University, Shanghai, China. [4]Department of Pathology, West China Hospital, Sichuan University, Chengdu, China. [5]Lung Cancer Center, West China Hospital, Sichuan University, Chengdu, China. [6]INSERM, U1065, Equipe 12, Centre Méditerranéen de Médecine Moléculaire (C3M), Nice, France. [7]Université Côte d'Azur, Nice, France. [8]These authors contributed equally: Haoning Peng, Zhile Wang, Mengyao Wang. ✉e-mail: lunxu_liu@aliyun.com; shensi.sean@gmail.com

ASCL1+ neuroendocrine (SCLC-A), NEUROD1+ neuronal (SCLC-N), and POU2F3+ tuft-like (SCLC-P) cell states[6]. A fourth subset lacking ASCL1, NEUROD1, and POU2F3 expression, termed triple-negative, YAP1+, mesenchymal, or inflammatory (SCLC-Y/I), represents an inflammatory non-NE phenotype. High-NE subtypes such as SCLC-A (~70%) and SCLC-N (~15%) are generally sensitive to frontline chemotherapy, whereas low-NE states, including SCLC-P (7–15%) and SCLC-Y or -I (3–10%), exhibit greater chemoresistance but enhanced immune infiltration[6]. Human tumours exhibit dynamic NE to non-NE transitions during adaptive resistance and relapse[2], a phenomenon mirrored in genetically engineered mouse models (GEMMs). However, genomic studies reveal minimal mutational differences between treatment-naïve and relapsed SCLC[7–10], underscoring the role of non-genetic plasticity in drug resistance. Recent work has identified transcriptional and epigenetic mechanisms governing these transitions: c-MYC-driven Notch activation promotes sequential evolution from SCLC-A to SCLC-N and YAP1+ non-NE states[11], while loss of Kdm1a, Kdm5a, or KDM6A facilitates NE-to-non-NE reprogramming through chromatin remodelling and ASCL1 suppression[12–14]. Beyond transcriptional and epigenetic regulation, post-transcriptional mechanisms are also increasingly recognized as key mediators of SCLC plasticity.

The mRNA-binding protein ZFP36L1 inhibits ASCL1 expression by binding to SOX2 and INSM1, driving a non-NE cell state reminiscent of SCLC-I tumours, highlighting the role of mRNA-level regulation in SCLC cell state transition[15]. While transcriptional regulation in SCLC has been extensively studied, mRNA translational regulation remains in its infancy. The initiation phase of mRNA translation, regulated by multiple initiation factors, is important for adjusting the proteome in cancer cell plasticity[5]. Among others, eIF4E, the cap-binding protein in eIF4F complex, and eIF4A, an RNA helicase, play critical roles in oncogenesis by modulating specific mRNA translation[16]. In addition, eIF6 governs 60S ribosomal subunit maturation and assembly into functional 80S ribosomes by acting as an anti-association factor, holding 60S subunits in a translationally inactive state until release factors Shwachman-Bodian-Diamond syndrome protein (SBDS) and elongation factor like GTPase 1 (EFL1) recycle them for translation[17]. Aberrant eIF6 expression is widely observed in cancers, including colorectal, head and neck, lung and ovarian cancer, with heterozygous loss of eIF6 shown to confer resistance to oncogene-induced transformation, emphasizing its key role in tumour growth and progression[18]. Furthermore, eIF6 phosphorylation by the RACK1-PKCβII complex downstream of RAS suggests its involvement in oncogenic signalling[19]. Despite these findings, the molecular mechanisms by which eIF6 contributes to cancer cell plasticity remain unclear.

Here, we identify a functional association between the translation initiation factor eIF6 and NE-to-non-NE transdifferentiation in SCLC. In non-NE cell states, increased expression of eIF6 partially dissociates from ribosomes and contributes to the assembly of integrin–FAK complexes and activation of the downstream MAPK pathway. Genetic perturbation of eIF6 limits non-NE transitions and increases SCLC sensitivity to frontline chemotherapy. Furthermore, in situ detection of eIF6 association with CD104/FAK complexes correlates with clinical outcomes in SCLC patients.

Results

SCLC neuroendocrine plasticity is associated with translational remodelling

To investigate additional mechanisms implicated in SCLC plasticity and drug resistance, we conducted a comparative analysis of gene expression profiles between relapsed SCLC patient samples post-chemotherapy ($n = 18$)[9] and treatment-naïve SCLC samples ($n = 81$)[20] using single-sample gene set enrichment analysis (ssGSEA)[21] (Fig. 1a). We observed enrichment in pathways related to eukaryotic translation and 60S ribosome regulation in relapsed samples (Fig. 1b), hinting at translation regulation in SCLC's chemotherapy tolerance. Intriguingly, pathways associated with NE cell states[22] are diminished in relapsed compared to treatment-naïve SCLC samples, raising the possibility that global alterations in mRNA translation may represent a common feature of NE transdifferentiation (Fig. 1c). Similar enrichment patterns, including ribosome 60S large subunit biogenesis, cytoplasmic translation, and ribosome assembly, were observed in *ASCL1*^{low}/*NEUROD1*^{low} non-NE SCLC cells[23] that are refractory to chemotherapy and anti-PD-L1 immunotherapy in the IMpower133 trial (Fig. 1d and Supplementary Fig 1a)[3]. Meanwhile, neuroendocrine-associated pathways, such as neurotransmitter secretion, synaptic vesicle exocytosis and axoneme assembly, were enriched in NE SCLC subtypes (Fig. 1d). To validate these in silico findings, we assessed mRNA translational activity in distinct cell state transition models across multiple SCLC cell lines (Fig. 1e). These include the spontaneous transition model from MYCL^{high}/ASCL1^{+} H209 cells to non-NE H209A cells, hepatocyte growth factor (HGF)-induced transition models[24] involving MYCN^{high}/ASCL1^{+} H69 cells (H69 vs YAP1^{+}H69M) or H209M cells (Fig. 1e), chemotherapy-resistant cell lines (NEUROD1^{+} H82 vs c-Myc^{high} H82R)[25] (Fig. 1e). In these transdifferentiated or chemotherapy-refractory cell states, we observed variant non-NE phenotypes, ranging from smaller, less compact suspension cell clusters to fully attached, spread-out mesenchymal cell morphologies (Fig. 1e).

Consistent with transcriptomic analyses, non-NE cells exhibited a significant alteration in translation activity compared to their NE counterparts, as revealed by polysome profiling[26]. Ultracentrifugation of cell lysates on a sucrose gradient indicated a reduced content of polysome-bound mRNAs in variant non-NE cells compared to NE cells (Fig. 1f). This was evident by the decreased ratio of the area under curve (AUC) between polysome (ribosomes ≥ 2) and monosomes (40S-80S) (Supplementary Fig. 1b), as shown by multiple models (Fig. 1f, right), suggesting a global downregulation of translational activity in variant non-NE SCLC cells. Moreover, the reduced translation activity is not due to reduced cell proliferation as evidenced by CCK-8 cell number count during three days (Supplementary Fig. 1c). In line with these findings, variant non-NE cells across multiple models showed increased tolerance to carboplatin/etoposide combination treatment (Fig. 1g). We also observed downregulation of translation activity in two mesenchymal-like YAP1-high thoracic tumours, H196 (RB1/TP53 mutant) and DMS114 (SMARCA4 mutant) cells (Supplementary Fig. 1d, e). Transcriptomic pathway analysis further confirmed the transdifferentiated non-NE states, showing increased EMT pathway, inflammatory responses (TNFα signalling pathway and interferon-α response) across non-NE cell states from multiple models (Supplementary Fig. 2a). Alongside these polysome profile changes, we also noted an increase in the phosphorylation of RPS6 (p-RPS6) in non-NE SCLC cells compared to NE cells (Supplementary Fig. 2b). This elevated p-RPS6 consistently associated with poly-ribosomes in non-NE cell lysates (Supplementary Fig. 2c), whose dephosphorylation is recognized as necessary for actively translating ribosomes[27]. Given the central role of the mTOR pathway in regulating RPS6 phosphorylation and mRNA translation, we assessed its activation by monitoring phosphorylation of p70 S6K1 (Thr389), 4EBP1 (Ser65), and AKT across SCLC transdifferentiation models. As shown in Supplementary Fig. 2b, phosphorylation of S6K1 and 4EBP1 remained largely unchanged, while p-AKT showed a modest increase only in the H69 model. These findings suggest that mTOR signalling is unlikely to account for the elevated p-RPS6 observed in non-NE cell states.

Translation landscape in NE versus non-NE SCLC

To characterize the translational landscape underlying NE-to-non-NE transition in SCLC, we performed genome-wide polysome profiling across HGF-induced (H69 vs. H69M), spontaneous (H209 vs. H209A), and chemotherapy-mediated (H82 vs. H82R) cell state models to identify mRNAs subject to altered translational regulation (Fig. 2a and Supplementary Fig. 3a and 3d). Polysome-associated RNA sequencing

https://doi.org/10.1038/s41467-026-69899-8

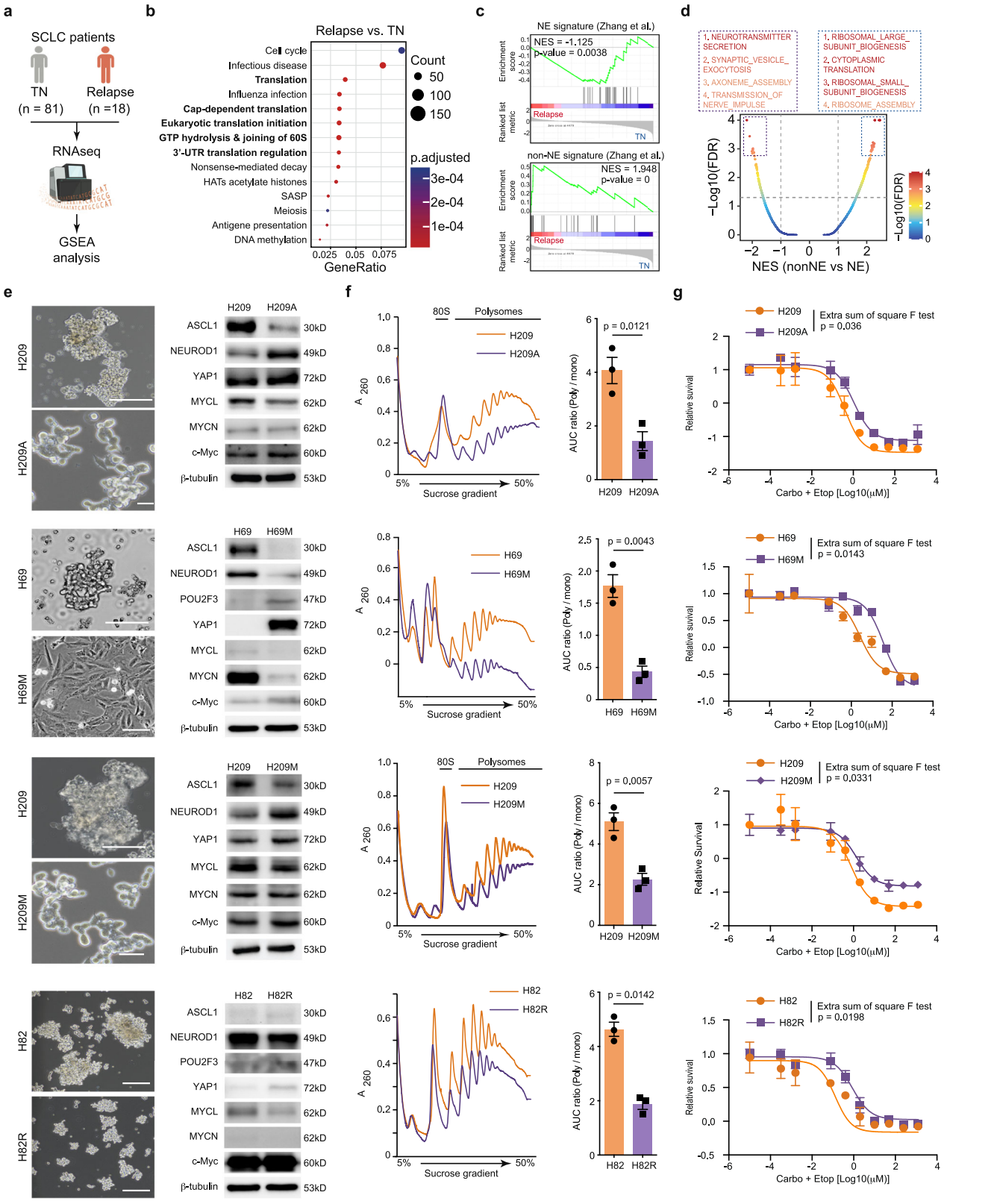

in H69M and H69 cells allowed us to categorize mRNAs into three distinct groups: Group 1 displayed at least a twofold change in cytoplasmic mRNA levels but less than a twofold change in polysomal mRNA levels (Fig. 2b, blue points); Group 2 exhibited at least a twofold change in polysomal mRNA levels but less than a twofold change in cytoplasmic mRNA levels (Fig. 2b, orange points); and Group 3 showed at least a twofold change, either an increase or decrease, in both cytoplasmic and polysomal mRNA levels (Fig. 2b, green points). This paired transcription-translation analysis revealed substantial alterations in translational regulation along the spectrum of SCLC transdifferentiation. Similar findings were replicated in H82 and H209 models (Supplementary Fig. 3b, 3e and Supplementary Data 1). Cumulative gene expression analysis of both ribosome-bound mRNAs and total RNAs showed stronger regulatory effects at the level of polysome-

Fig. 1 | Global downregulation of translation activity in chemorefractory non-NE SCLC cell state. a Gene expression analysis of tumour samples from treatment-naïve and relapsed SCLC patients. Created in BioRender. Shen, S. (2026) https://BioRender.com/5p1ea8h. **b** Single-sample Gene Set Enrichment Analysis (ssGSEA) of pathways in relapsed ($n = 18$) versus treatment-naïve ($n = 81$) SCLC tumours. Enrichment was assessed by normalized enrichment score (NES, one-sided), and significance was determined by FDR-adjusted q-value. **c** GSEA analysis of NE and non-NE gene signatures in relapsed and treatment-naïve samples; $n = 18$ relapsed patient samples and $n = 81$ treatment-naïve patient samples. **d** Volcano plot of ssGSEA analysis highlighting pathways involved in non-NE and NE SCLC tumours from the RNA-seq dataset of IMpower133 human SCLC cohort ($n = 271$); **e** Bright-field images of different SCLC cell models and the corresponding immunoblot analysis assessing the expression of SCLC cell state markers. For H209/H209A, the samples derive from the same experiment, but different gels for ASCL1, c-Myc, another for MYCL, another for MYCN, another for NEUROD1, YAP1 and β-tubulin were processed in parallel. For H69/H69M, the samples derive from the same experiment but different gels for ASCL1 and MYCN, another for NEUROD1 and YAP1, another for MYCL, another for POU2F3, another for c-Myc, another for β-tubulin were processed in parallel; For H82/H82R, the samples derive from the same experiment but different gels for ASCL1 and MYCN, another for NEUROD1, YAP1 and β-tubulin, another for MYCL, another for c-Myc, another for POU2F3 were processed in parallel; For H209/H029M, the samples derive from the same experiment but different gels for ASCL1, another for YAP1, another for MYCL, another for MYCN, another for c-Myc, another for NEUROD1 and β-tubulin were processed in parallel. Blots are representative of $n = 3$ biologically independent experiments. **f** Polysome profiling analysis assessing translation activity across multiple models. The ratio of the area under curve (AUC) between polysome and monosome fractions was calculated using an *in-house* MATLAB script. Polysome profiles are representative of $n = 3$ biologically independent experiments for each cell model. Statistical significance was assessed using a two-sided unpaired Wilcoxon rank-sum test. **g** CCK-8-based cell viability analysis across multiple SCLC models. Cells were treated with carboplatin (Carbo) and etoposide (Etop) for 72 h at the indicated doses. The one-sided extra-sum of square F test was used for statistical analysis of $n = 3$ biologically independent experiments.

associated mRNAs (Fig. 2c). Notably, differentially transcribed (ΔmRNA, FDR < 1% and $\log_2|FC| > 1$) and translated mRNAs (Δtranslation efficiency [ΔTE], FDR < 10%) were largely independent, with minimal overlap between transcriptional and translational changes associated with the non-NE cell state (Fig. 2d and Supplementary Fig. 3b and 3e). Specifically, The SCLC neuroendocrine signature[22] was downregulated at both transcriptional and translational levels in H69 cell model (Fig. 2e); Similar changes were also observed in the other two models (Supplementary Fig. 3c and 3f). We selected H69 as a representative model to further examine the 5′ untranslated regions (5′ UTRs) of differentially translated and transcribed mRNAs (Fig. 2f). Transcripts upregulated at the translational level in non-NE cell states exhibited lower GC content and increased 5′UTR length, whereas translationally downregulated transcripts had higher GC content and shorter 5′UTR length (Fig. 2f). Of note, reduced GC content in 5′UTR has been linked to enhanced translation under conditions of translational perturbation, though these features alone may not be sufficient to mediate translational control[28].

The observed global downregulation of translation in the non-NE cell state may be linked to alterations in ribosome scanning or composition, potentially triggered by the cellular stress response[29,30]. To investigate these possibilities, we first measured ribosome transit rates using a harringtonine run-off assay (Supplementary Fig. 3g)[31]. Treatment with harringtonine in both NE and non-NE cells led to a reduction of polysomes and an accumulation of 80S ribosomes (Supplementary Fig. 3h), thereby ruling out ribosome stalling as the primary cause of the global translation remodelling. To further explore potential changes in ribosomal composition, we subsequently employed quantitative high-coverage tandem-mass-tag (TMT) mass spectrometry on H69 and H69M cells to evaluate the expression of all ribosome proteins (RPs)(Fig. 2g and Supplementary Fig. 4a)[32]. Cells were fractioned using sucrose gradient sedimentation, and monosomes (M, a single ribosome), light polysomes (LP, 2-4 ribosomes), and heavy polysomes (HP, ≥ 5 ribosomes) were collected from both H69 and H69M cells (Fig. 2g). On average, we detected peptides predominantly in the range of 8–20 amino acids, with a high protein coverage (Supplementary Fig. 4b–d and Supplementary Data 2). A diverse array of subcellular proteins potentially associated with polysomes was detected, with a substantial proportion belonging to nuclear proteins (37%) (Supplementary Fig. 4e). Gene ontology analysis showed an enrichment of translation-related components in our mass spectrometry analysis (Supplementary Fig. 4f). Differential proteomic analysis demonstrated distinct protein expression profiles associated with ribosomes in each sub-fraction (Supplementary Fig. 4g). Moreover, principal component analysis highlighted a clear segregation between NE and non-NE cell states, emphasizing translation remodelling during SCLC transdifferentiation (Fig. 2h). Intriguingly, despite the global downregulation of translation in the non-NE cell state compared to the NE cell state, the average composition of RPs within monosomes, light polysomes, and heavy polysomes remained largely invariant (Fig. 2i). These findings suggest that translation alterations associated with SCLC transdifferentiation are likely driven by regulatory mechanisms beyond ribosome stalling or modifications in ribosomal protein composition.

Translation initiation factor eIF6 is upregulated in the non-NE cell state

As neither mTOR pathway activity, ribosomal components, nor ribosome stalling showed substantial changes during SCLC transdifferentiation, we next examined whether translation initiation, the rate-limiting step of protein synthesis, contributes to the observed translational plasticity in SCLC. Intriguingly, we observed a discernible increase in the abundance of the 60S ribosomal subunit in the non-NE cell state compared to NE cell state (Fig. 1). eIF6 interacts with nascent 60S subunits, facilitating their assembly with 40S subunits to form active 80S ribosomes[33]. Notably, elevated eIF6 levels in c-Kit+ bone marrow cells reduce the 80S:60S ratio, leading to translational inactivation of 80S ribosomes[17]. This identifies eIF6 as a rate-limiting factor in tumorigenesis, as evidenced by studies in *Eif6*$^{+/-}$ mouse embryonic fibroblasts, which show reduced transformation capacity[18]. Among key translation initiation factors, we found that eIF6 was the only factor consistently upregulated at the protein (Fig. 3a and Supplementary Fig. 5a) and mRNA level (Fig. 3b and Supplementary Fig. 5b) during non-NE transition across multiple SCLC models.

Given the observed alteration of eIF6 expression in multiple in vitro transdifferentiation models, we investigated whether this phenomenon occurs in vivo and in patient samples. We first analysed a public dataset of SCLC patient samples[20], categorizing them into four groups based on the expression of classical NE-associated TFs, namely ASCL1^{high}, NEUROD1^{high}, dual-positive (ASCL1^{high}NEUROD1^{high}) and dual-negative (ASCL1^{low}NEUROD1^{low}). Notably, eIF6 expression was significantly elevated in dual-negative samples, suggesting an inverse relationship between eIF6 expression and the NE cell state (Supplementary Fig. 5c). Meanwhile, *MYC*, a known driver of SCLC transdifferentiation[34], was also upregulated in non-NE tumours (Supplementary Fig. 5c). On the other hand, despite the observed inverse correlation between eIF6 and NE cell state, eIF6-associated proteins *SBDS* and *EFL1* expression levels remained unchanged (Supplementary Fig. 5d). Further supporting these findings, we observed increased *Eif6* and *Myc* expression, along with decreased *Ascl1* expression, in murine RPM tumours compared to RPR2 (*Rb1*$^{fl/fl}$/*Trp53*$^{fl/fl}$/*Rbl2*$^{fl/fl}$) tumours (Supplementary Fig 5e, f). This aligns with previous reports of reduced

https://doi.org/10.1038/s41467-026-69899-8

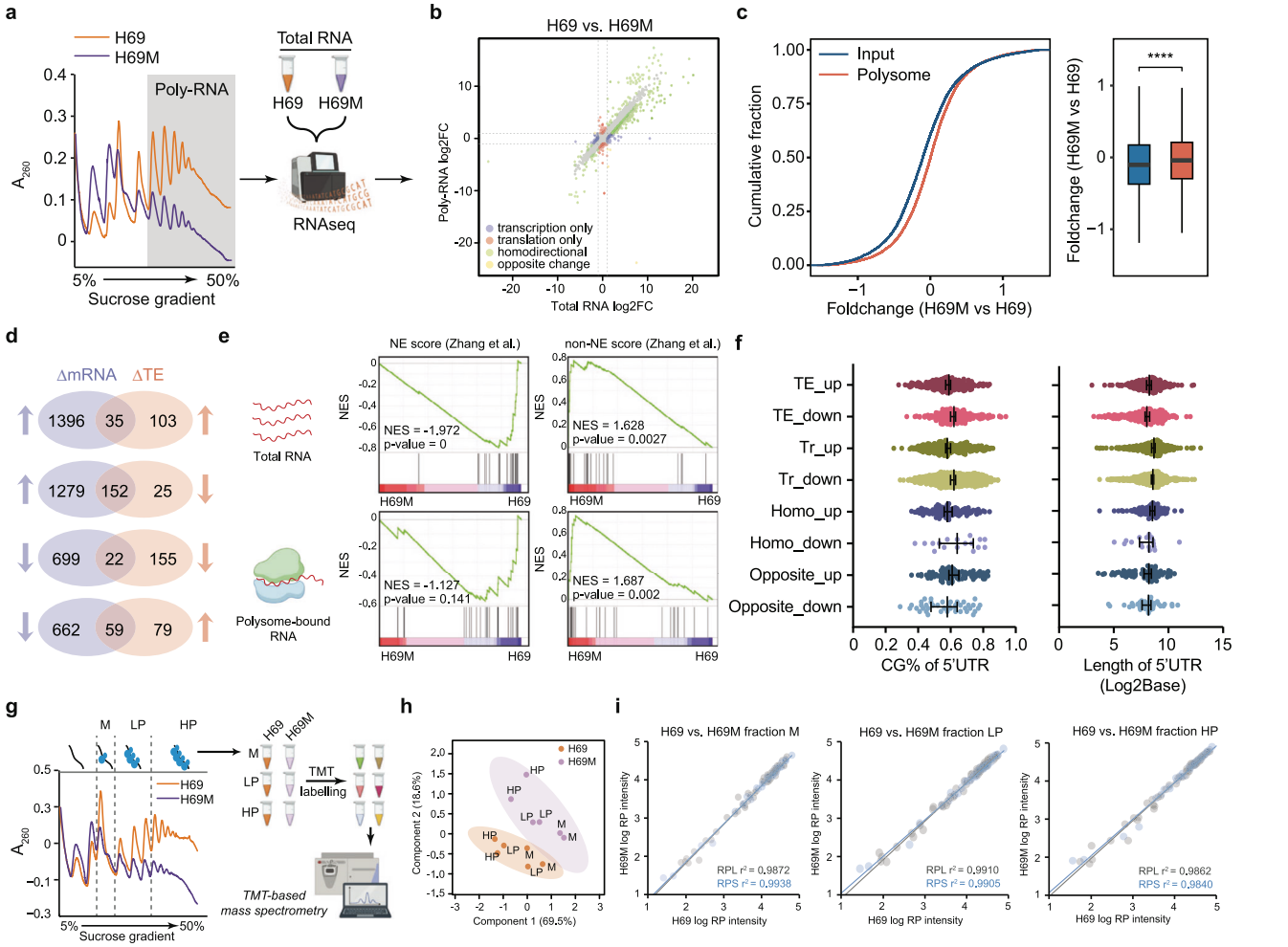

Fig. 2 | Altered translational landscape during SCLC transition from NE to non-NE cell state. a Integrated polysome-associated mRNA sequencing (Poly-RNA-seq) and total RNA sequencing (RNA-seq) analyses in H69 and H69M cells. Created in BioRender. Shen, S. (2026) https://BioRender.com/5p1ea8h. **b** Genome-wide transcriptional and translational profiling comparing H69 and H69M cells. Genes with adjusted $p < 0.05$ and fold change > 2 (DESeq2) are colour-coded; $n = 3$ biologically independent experiments per group for both Poly-RNA-seq and RNA-seq. Differential translational efficiency was analysed using Xtail, with significance determined by one-sided Benjamini–Hochberg FDR-adjusted p values. **c** Empirical cumulative distribution function plots showing fold changes of transcripts detected in both polysome-associated RNAs and total RNAs (left), and boxplots comparing fold changes between conditions (right). Analyses were performed using data from three independent polysome profiling experiments, as in (**b**). **d** Venn diagrams showing differentially transcribed genes (ΔmRNA, $\log_2$ fold change > 1) and differentially translated genes (Δ translational efficiency, ΔTE) between H69M and H69 cells. **e** Gene set enrichment analysis (GSEA) of NE and non-NE gene signatures in total RNAs (transcriptome) and polysome-bound RNAs (translatome) comparing H69M and H69 cells. Created in BioRender. Shen, S. (2026) https://BioRender.com/5p1ea8h. **f** Analysis of 5′UTR features of transcripts regulated at transcriptional (Tr) and translational (TE) levels. Homo, concordant changes at both levels; Opposite, discordant changes. Each dot represents one transcript (Supplementary Data 3). Genes shown were identified using xtail with $n = 2$ biological replicates, and 5′UTR length and GC content represent gene-intrinsic features analysed at the gene level. Error bars indicate mean ± SEM. Statistical significance was assessed using a two-sided unpaired t-test with Welch's correction. **g** Schematic of TMT-based mass spectrometry analysis of ribosomal fractions from H69 and H69M cells. Polysome profile is representative of $n = 2$ biologically independent experiments for TMT-mass spectrometry analysis. M, monosome; LP, light polysome; HP, heavy polysome. Created in BioRender. Shen, S. (2026) https://BioRender.com/5p1ea8h. **h** Principal component analysis (PCA) of ribosomal fractions from H69 and H69M cells. The analysis is performed based on $n = 2$ biologically independent sample collections. **i** Log_2-transformed, median-centred ribosomal protein (RP) intensities from $n = 2$ biologically independent replicates in M (left), LP (middle), and HP (right) fractions. Large-subunit RPs are shown in grey and small-subunit RPs in blue. Linear regressions and Pearson correlation coefficients are shown.

NE marker expression in invasive RPM tumours compared to RPR2 tumours[11]. To extend these observations, we performed immunohistochemistry of Eif6 and Ascl1 expression in the RPM mouse model, which exhibits NE-low histopathology[34]. Adenoviruses carrying *Cre*-driven by the neuroendocrine *calcitonin gene-related peptide* (*Cgrp*) promoter were nasally administered to mice (Fig. 3c), and micro-computed tomography revealed centrally located tumours with increased density at major bronchi between weeks 5 and 7 post-infection (Fig. 3c, top). Tumours were collected at various stages, including in situ carcinoma (402), locally advanced tumours (412), and locoregional metastatic tumours (404) (Fig. 3c). In in situ carcinoma, Ascl1 expression was high, while Eif6 was largely absent (Fig. 3d, 402). Similarly, in the locally advanced tumour, eIF6 expression remained low in regions with high Ascl1 expression (Fig. 3d, 412). However, in more advanced tumours, eIF6 staining was intensified in Ascl1-low regions, contrasting with lower eIF6 expression Ascl1-high regions (Fig. 3d, 404). To determine whether this inverse correlation between eIF6 and the NE cell state extends to human tumours, we analysed surgical specimens from limited-stage SCLC patients ($n = 38$). Multiplex immunofluorescence (mIF) was performed on formalin-fixed, paraffin-embedded (FFPE) samples to simultaneously detect ASCL1, NEUROD1, and eIF6 (Fig. 3e). Single-cell protein quantification using

https://doi.org/10.1038/s41467-026-69899-8

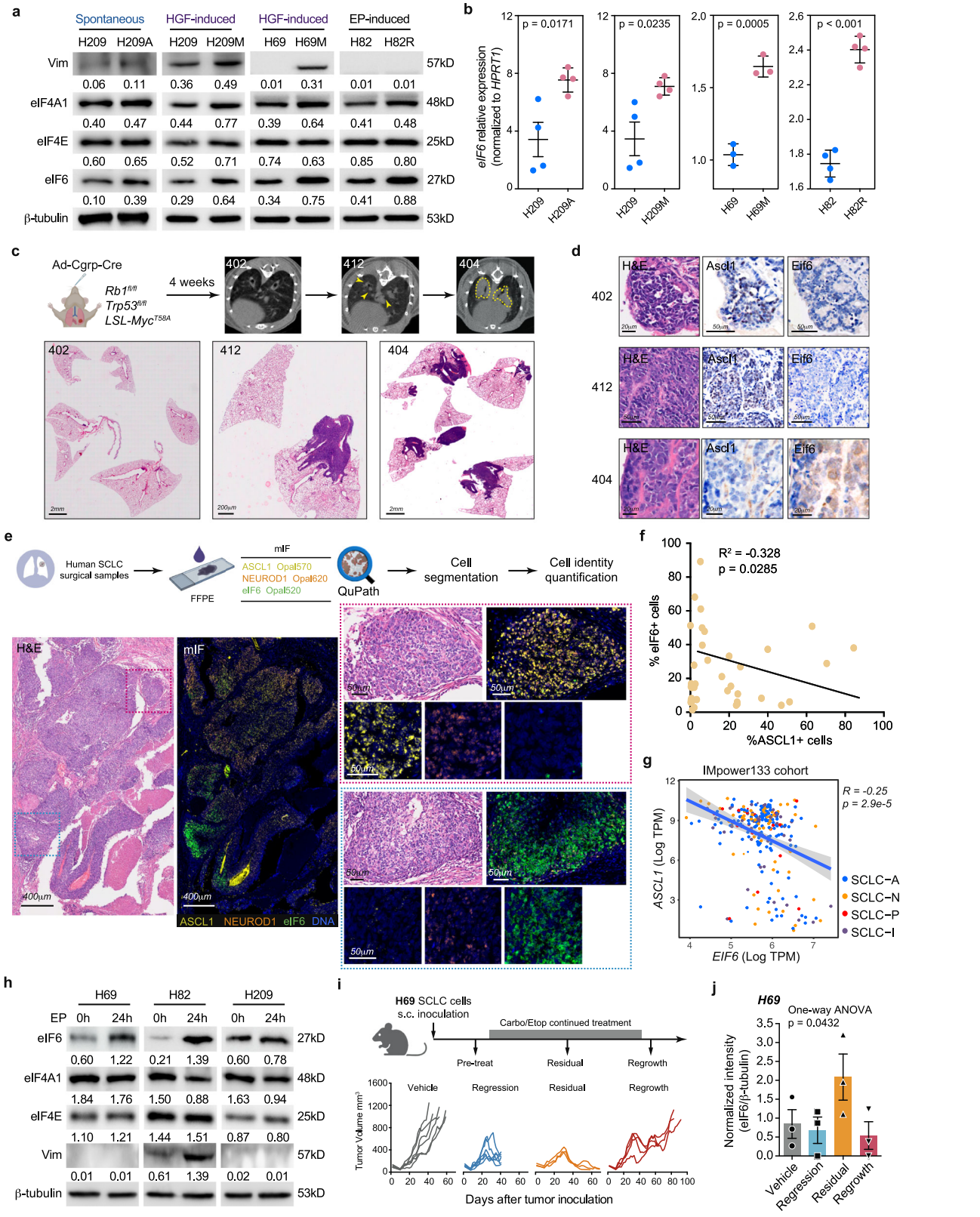

QuPath software (Fig. 3e and Supplementary Fig. 6a)[35] revealed significant intra-tumoral heterogeneity in ASCL1, NEUROD1, and eIF6 expression. Despite this variability, eIF6 and ASCL1 expression were inversely correlated ($R^2 = -0.328$, p-value = 0.0285), consistent with our in vitro and murine findings (Fig. 3f and Supplementary Fig. 6b). However, we acknowledge that explicit cell-classification-based quantification of ASCL1 and eIF6 expression, aimed at assessing their co-expression, would be valuable for defining the relationship between these two proteins at the patient level. Definitely resolving their expression patterns in individual cells will require higher-resolution spatial single-cell transcriptomic and proteomic approaches in the future. Nevertheless, the anti-correlation between ASCL1 and eIF6 was further supported by RNA sequencing data from the IMpower133 cohort[36] (Fig. 3g), and a similar inverse trend–although not reaching

Fig. 3 | Elevated expression of eIF6 in chemoresistant non-NE cell state. a. Immunoblot analysis of translation initiation factor expression across multiple SCLC models. β-tubulin was used as a loading control. Blots are representative of $n = 3$ biologically independent experiments. For H69/H69M and H82/H82R, the samples derive from the same experiment but different gels for vimentin, another for eIF4E, another for eIF6, another for eIF4A1 and β-tubulin were processed in parallel; For H209/H209A, the samples derive from the same experiment but different gels for eIF4E, another for eIF6, another for eIF4A1, another for vimentin and β-tubulin were processed in parallel; For H209/H209M, the samples derive from the same experiment but different gels for eIF4E, another for eIF4A1, another for vimentin, another for eIF6 and β-tubulin were processed in parallel. **b** Quantitative PCR analysis of EIF6 mRNA expression across paired SCLC cell models. Error bars represent mean±s.d. from $n = 3$ or 4 independent experimental replicates, as indicated. Statistical significance was assessed using a two-sided unpaired Wilcoxon rank-sum test. **c** Representative micro-CT and H&E staining images of RPM mice showing lung tumour formation (yellow circles) following intranasal infection with Ad5-Cgrp-Cre. Each group was analysed by micro-CT and H&E staining in $n = 3$ biologically independent mice. Created in BioRender. Shen, S. (2026) https://BioRender.com/5p1ea8h. **d** H&E and immunohistochemistry (IHC) staining for ASCL1 and EIF6 in RPM tumours at different stages. Each group was analysed in three biologically independent mice. **e** Multiplex immunofluorescence (mIF) analysis of human SCLC surgical samples. Images were analysed using QuPath to quantify the percentage of $ASCL1^+$, $NEUROD1^+$ and $EIF6^+$ cells (top). Representative mIF and H&E images from the same tumour are shown below, illustrating the spatial distribution of ASCL1, NEUROD1 and EIF6. Insets show magnified regions of interest. mIF images are representative of $n = 38$ patient FFPE samples. Created in BioRender. Shen, S. (2026) https://BioRender.com/5p1ea8h. **f** Pearson correlation analysis between the number of $EIF6^+$ and $ASCL1^+$ cells across 38 human SCLC tumours. **g** Pearson correlation analysis of EIF6 and ASCL1 expression levels in human SCLC samples from the IMpower133 cohort ($n = 271$). The shaded area indicates the 95% confidence interval of the regression line. **h** Immunoblot analysis showing chemotherapy-induced EIF6 expression and key translation initiation factors across multiple SCLC cell models. β-tubulin was used as a loading control. Carbo, carboplatin (10 μM); Etop, etoposide (2 μM). Blots are representative of $n = 3$ biologically independent experiments performed on separate cell preparations with similar results. For H69, the samples derive from the same experiment but different gels for eIF4A1 and eIF4E, another for eIF6, another for vimentin and β-tubulin were processed in parallel. For the other two cells, the samples derive from the same experiment but different gels for eIF4A1 and eIF4E, another for eIF6, vimentin and β-tubulin were processed in parallel. **i** H69 xenograft tumours were harvested at four time points during chemotherapy (carboplatin 60 mg kg^{-1} plus etoposide 12 mg kg^{-1}, i.p., weekly) (top). Individual tumour growth curves corresponding to each biopsy time point are shown below. Tumour growth curves are from $n = 6$ (vehicle), $n = 6$ (regression), $n = 3$ (residual) and $n = 4$ (regrowth) mice. Created in BioRender. Shen, S. (2026) https://BioRender.com/5p1ea8h. **j** Quantification of EIF6 protein levels by immunoblotting in tumours collected at the four time points shown in (**i**). Error bars represent s.d. from $n = 3$ mice per group.

statistical significance–was also observed in treatment-naïve samples from the George et al. dataset[20] (Supplementary Fig. 5g).

Frontline chemotherapy induces eIF6 expression

Reanalysis of the transcriptomic dataset shown in Fig. 1a revealed that an inverse correlation between *eIF6* and *ASCL1* (Supplementary Fig. 7a, b), while *eIF6* expression showed a modest positive correlation with *POU2F3* and *MYC*, but not with *NEUROD1* (Supplementary Fig. 7b). Stratification of patient samples further demonstrated elevated *eIF6* expression in *ASCL1*-low relapsed tumours compared with treatment-naïve counterparts (Supplementary Fig. 7c), other translation initiation factors, including *EIF4E*, *EIF4G1* and *EIF4A*, were either downregulated or unchanged in relapsed samples, consistent with our in vitro findings across transdifferentiation models (Supplementary Fig. 7c). Carboplatin/etoposide treatment acutely increased eIF6 protein levels in human SCLC cell lines, as confirmed by western blot (Fig. 3h), and these levels remained elevated in time-course assays across human and RPM-derived mouse models[34] (Supplementary Fig. 7d). To validate these observations in vivo, we examined *EIF6* expression in a residual disease setting. Human H69 (Fig. 3i) and H82 (Supplementary Fig. 7f) tumours transplanted into *Balb/cNj-Foxn1^{nu}/Gpt* mice were treated with carboplatin/etoposide for three cycles. Tumours initially regressed but relapsed around day 60 following a minimal residual disease phase (Fig. 3i and Supplementary Fig. 7f). Notably, eIF6 protein expression was selectively upregulated during the residual phase in both models (Fig. 3j and Supplementary Fig. 7e and 7g-h), mirroring our in vitro observations.

eIF6 regulates non-NE transdifferentiation across multiple models

To assess the functional role of eIF6 upregulation in SCLC neuroendocrine plasticity, we examined the effects of eIF6 knockdown in non-NE SCLC cells. We did not observe significant alterations of translation activity in H69 and H69M cells upon eIF6 knockdown (Supplementary Fig. 8a). RNA sequencing followed by GSEA revealed that eIF6 knockdown in H69M cells significantly downregulated epithelial-mesenchymal transition (EMT)-associated gene signatures (Fig. 4a, top), including *NOTCH* family proteins, integrins, and vimentin, all of which have been implicated in EMT-driven transdifferentiation in SCLC (Fig. 4b, left and Supplementary Data 3). Conversely, eIF6 knockdown led to a marked increase in the neuroendocrine gene signature[15,37] (Fig. 4a, bottom and Supplementary Data 3), encompassing *HES6, TOP2A, DLL3, NEUROD1, ASCL1, INSM1* and *CHGA* (Fig. 4b, right). To substantiate these findings, we performed transcriptomic analyses in the spontaneous transdifferentiation model H209A (Supplementary Fig 8b, c) and the chemotherapy-induced model H82R (Supplementary Fig 8d, e). Both models showed downregulation of EMT-associated signatures and upregulation of SCLC neuroendocrine programs. Consistent with these findings, western blot analysis across the three SCLC cell models showed a reduction in EMT-related transcription factors ZEB1/2 in non-NE cell state, although the effect was less pronounced in H82R cells. Partial restoration of ASCL1 expression was also observed in H209A and H82R cells, with a weaker effect in H69M cells (Fig. 4c).

Although eIF6 knockdown does not fully reverse non-NE transdifferentiation, these results suggest that its inhibition may restrain the transition toward a non-NE state across distinct transdifferentiation contexts. While global polysome profiles remained unchanged (Supplementary Fig. 8a), selective translational control might also underlie the observed phenotypic effects. We therefore performed ribosome profiling (Ribo-seq) to assess ribosome scanning and mRNA-specific translation upon eIF6 knockdown (Supplementary Data 4). Ribo-seq displayed canonical features, including 26–29 nt footprints, strong frame 0 enrichment, and clear three-nucleotide periodicity (Supplementary Fig. 8f-h). Notably, eIF6 depletion primarily induced ribosome stalling within the first 20-45 codons downstream of the start codon, consistent with its known anti-association activity (Supplementary Fig. 8i). Analysis of translation efficiency revealed that eIF6 knockdown predominantly affected mRNAs encoding RNA processing factors involved in splicing and ribosome biogenesis (Supplementary Fig. 8j), with only a limited set of selectively translated proteins, including WDR75, MARK3, MSN, PABPC1, and PPIG (Supplementary Data 4). No established regulators of SCLC non-NE transdifferentiation exhibited altered translation under these conditions.

We next performed a transdifferentiation assay using human H69 cell lines, which are known to transition into a non-NE cell state upon HGF treatment[24]. As shown in Fig. 4d, H69 cells expressing non-targeted control shRNA (sh_NTC) exhibited increased adhesion upon HGF treatment, as visualized by crystal violet staining. In contrast, eIF6 knockdown dramatically impeded this phenotypic change, maintaining cells in neuroendocrine spheroid aggregates in suspension and leading to a reduced crystal violet staining signal (Fig. 4d). A similar

https://doi.org/10.1038/s41467-026-69899-8

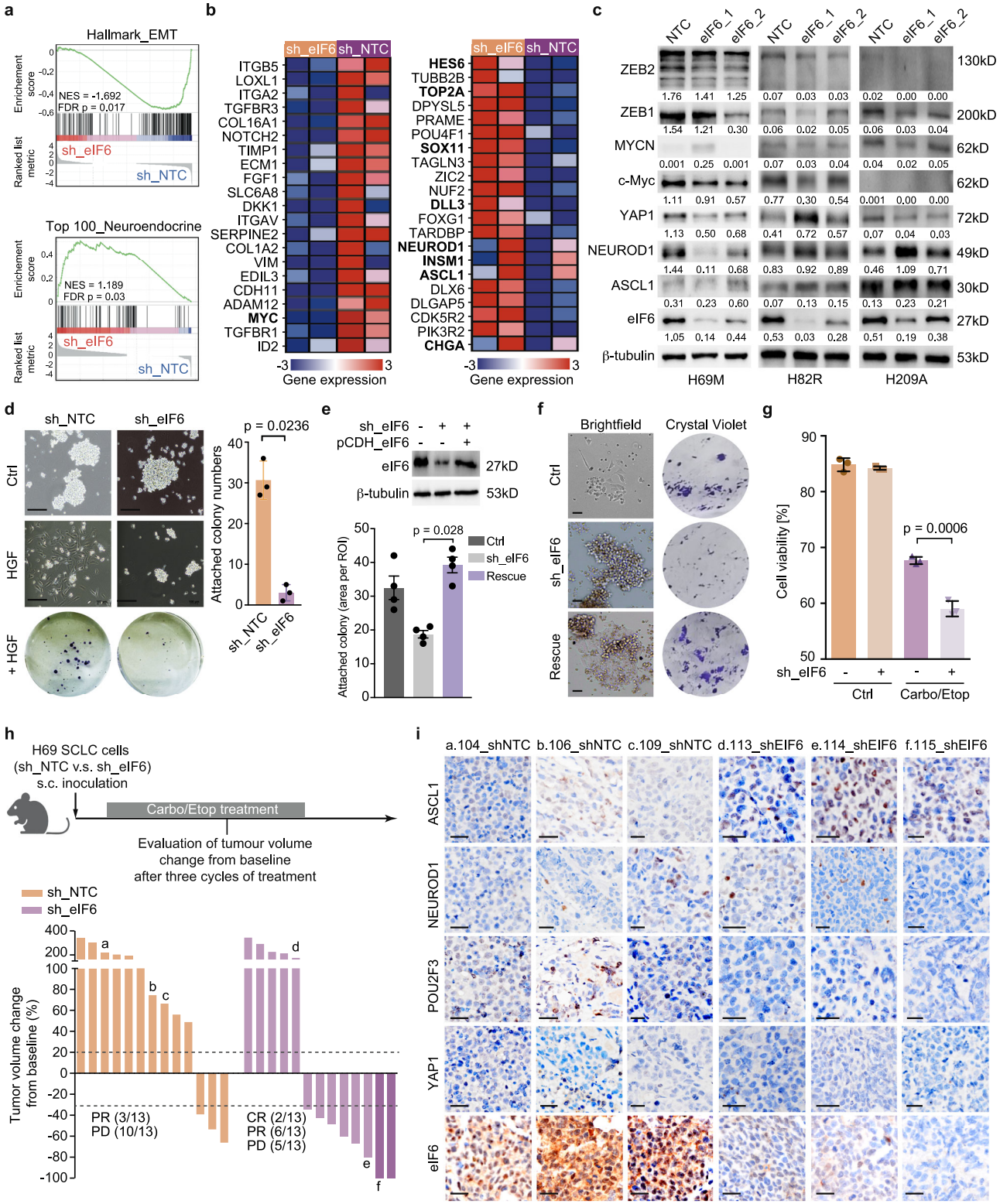

inhibitory effect of eIF6 knockdown was observed in EZH2 inhibitor-mediated SCLC transdifferentiation[38] (Supplementary Fig. 9a). To further explore these findings, we performed a transdifferentiation assay[14] using RPM-derived mouse SCLC cell lines. RPM-derived cells progressively and spontaneously shifted from neuroendocrine spheroid growth to a non-neuroendocrine adherent state[34] 9b), accompanied by reduced EMT-associated factors and partial restoration of ASCL1 expression (Supplementary Fig. 9c). Re-expression of shRNA-resistant eIF6 restored HGF-induced transdifferentiation (Fig. 4e, f), confirming an on-target effect. Conversely, lentiviral eIF6 overexpression in NE-state cells (H69, H82, and H209) enhanced HGF-induced attachment (Supplementary Fig. 9d–f). Together, these data indicate that eIF6, while not a primary driver, contributes to the non-NE transition in SCLC.

Intervention of eIF6 sensitizes SCLC to chemotherapy

Given the heightened sensitivity of neuroendocrine-state SCLC to platinum-based chemotherapy[36], we investigated whether eIF6

Fig. 4 | eIF6 knockdown mitigates non-NE transition and improves sensitivity of SCLC to chemotherapy. a Enrichment of EMT and NE gene signatures following EIF6 knockdown in non-NE cell states. RNA-seq analysis is performed in $n = 2$ biologically independent samples. **b** Gene expression profiling of EMT- and NE-associated pathways upon EIF6 knockdown in non-NE cell states. RNA-seq analysis is performed in $n = 2$ biologically independent samples. **c** Immunoblot analysis of EMT-associated and NE proteins following EIF6 knockdown across multiple SCLC models. Blots are representative of $n = 3$ biologically independent experiments. For H69M, the samples derive from the same experiment but different gels for ZEB1, another for ZEB2, another for MYCN, another for YAP1, another for eIF6 and c-Myc, another for ASCL1, NEUROD1 and β-tubulin were processed in parallel; For H82R, the samples derive from the same experiment but different gels for ZEB2, ZEB1, MYCN and c-Myc, another for YAP1 and ASCL1, another for NEUROD1, eIF6 and β-tubulin were processed in parallel. For H209A, the samples derive from the same experiment, but different gels for ZEB2, ZEB1, MYCN and c-Myc, another for YAP1 and ASCL1, another for eIF6, another for NEUROD1 and β-tubulin were processed in parallel. **d** H69 cells with EIF6 knockdown were treated with HGF (40 ng mL^{-1}) for two weeks. Bright-field images show adherent growth (top). Attached colonies were stained with crystal violet for quantification ($n = 3$ biologically independent experiments). Scale bar, 100 µm. Error bars represent s.d. Statistical significance was assessed using a two-sided unpaired Wilcoxon rank-sum test. **e** Re-expression of shRNA-resistant wild-type EIF6 using pCDH lentivirus restores HGF-induced cell attachment in EIF6 knockdown cells. Top: immunoblot showing EIF6 knockdown and re-expression efficiency. Bottom, quantification of crystal violet–stained colonies ($n = 4$ independent experiments). Error bars represent s.d. Statistical significance was assessed using a two-sided unpaired Wilcoxon rank-sum test. **f** Representative images of H69 cells with EIF6 knockdown and re-expression after HGF treatment (40 ng mL^{-1}) for three weeks. Bright-field images (left) and crystal violet–stained colonies (right) are shown. Scale bar, 20 µm. **g** Live/dead cell analysis of shNTC and shEIF6 H69M cells treated with or without EP (carboplatin 10 µM and etoposide 2 µM) for 72 h, measured by flow cytometry. Data are mean ± SEM from $n = 3$ independent experiments. Statistical significance was determined using a two-sided unpaired Wilcoxon rank-sum test. **h** Chemotherapy sensitivity of subcutaneous xenografts derived from shNTC or shEIF6 H69 cells. Tumour volume changes were assessed after three chemotherapy cycles ($n = 13$ tumours per group). Response categories were defined as CR (−100%), PR (−30% to 0%) and PD (>20%). Lowercase letters indicate tumours used for immunohistochemistry in **i**. Created in BioRender. Shen, S. (2026) https://BioRender.com/5p1ea8h. **i** Representative immunohistochemistry images of ASCL1, NEUROD1, POU2F3, YAP1 and EIF6 in corresponding tumours from **h**. Scale bars, 50 µm.

knockdown could enhance chemotherapy responsiveness across multiple models. First, we assessed short-term chemotherapy effects in vitro. H69M cells were treated with carboplatin/etoposide for 72 hours, followed by flow cytometry analysis (Supplementary Fig. 9g). eIF6 knockdown significantly reduced the percentage of viable cells compared to the non-targeted controls upon chemotherapy (Fig. 4g). This effect was consistently observed in RPM-derived murine SCLC cell line, where *Eif6* knockdown led to increased cell death during short-term chemotherapy exposure (Supplementary Fig. 9h). Next, we examined long-term chemotherapy effects using a clonogenic assay[26]. RPM-derived mouse SCLC cells with *Eif6* knockdown exhibited not only reduced proliferation but also a substantial loss of residual survival cells, as indicated by a significant reduction in colony formation (Supplementary Fig. 9i). The enhanced chemotherapy response was further validated in vivo. H69 cell xenografts in *Balb/cNj-Foxn1^{nu}/Gpt* mice underwent three cycles of carboplatin/etoposide treatment. In the control group, 76.9% of mice (10/13) exhibited disease progression (PD) (Fig. 4h); In contrast, H69 xenografts with eIF6 knockdown demonstrated a marked response, with 61.5% (8/13) exhibiting disease regression, including two complete responses (CR) and six partial responses (PR) (Fig. 4h and Supplementary Fig. 9j). To explore the molecular underpinnings of this response, we collected FFPE tumour samples at the time of evaluation and performed immunohistochemistry of four key transcription factors associated with SCLC subtypes, including ASCL1, NEUROD1, POU2F3 and YAP1. Increased expression of POU2F3 (3/3) and, to a lesser extent, YAP1 (1/3) was observed in eIF6 control samples (sh_NTC), all of which showed PD at the time of evaluation (Figs. 4h, 4i, a–c). In contrast, tumours with eIF6 knockdown showed increased ASCL1 expression and low-to-absent levels of POU2F3 and YAP1 (Fig. 4i, d–f). Notably, one tumour (Fig. 4h, d) displayed lower ASCL1 expression, partial NEUROD1 expression, and low POU2F3 expression, correlating with relative chemotherapy resistance (Fig. 4i, d). Taken together, these findings suggest that targeting eIF6 suppresses non-NE transdifferentiation, thereby enhancing SCLC responsiveness to chemotherapy.

Reciprocal interplay between eIF6 and SCLC microenvironment

eIF6, a stress-responsive translation factor[39], was induced in non-NE SCLC states and upon chemotherapy exposure (Fig. 3), but its relationship with the tumour microenvironment remained unclear. Given that non-NE SCLC subtypes (SCLC-I) exhibit inflammatory signatures and lymphocyte infiltration[23], we examined whether eIF6 correlates with immune modulation. Cytokine profiling revealed increased secretion of GM-CSF, CXCL10 and CCL2 in non-NE H69M cells compared with H69 cells (Supplementary Fig. 10a), suggesting a pro-inflammatory secretome. In patient tumours, ASCL1-high regions displayed a "cold" phenotype with minimal lymphocytes and moderate CD68$^+$ macrophages, whereas eIF6-high regions, exhibiting desmoplastic features[40], were enriched for CD3$^+$ lymphocytes and CD68$^+$. 10b). This spatial pattern even persisted within the same tumour, where CD3$^+$ T cells localized selectively to eIF6-high but not ASCL1-high areas (Supplementary Fig. 10b, PT892). Analysis of the George et al. cohort[20] confirmed elevated IFNG and CD8A expression in eIF6-high tumours (Supplementary Fig. 10c), and CIBERSORTx deconvolution[41] further showed that CD8$^+$ T-cell fractions correlated with high eIF6 expression (Supplementary Fig. 10d), consistent with enhanced T-cell infiltration. To probe intercellular interactions, we re-analysed a published single-cell RNA-seq dataset using the original cell annotations[42] (Supplementary Fig 10e). This reanalysis recapitulated an inverse relationship between eIF6 and ASCL1 at single-cell resolution, except in tumours lacking *TP53* and/or *RB1* mutations (Supplementary Fig. 10f). CellChat inference[43] suggested that eIF6-high tumour cells interact with CD8$^+$ T cells via multiple ligand–receptor pairs (e.g., NECTIN2, MIF, LCK, collagens), while T cells signal back through the IFNG–IFNGR1 axis, suggesting possible environmental feedback on eIF6 expressing cells (Supplementary Fig. 10g). Functionally, eIF6 knockdown reduced PD-L1 expression in human and RPM-derived mouse models (Supplementary Fig. 10h, i), implicating eIF6-mediated regulation in immune evasion. In accordance with cell-cell communication analysis in Supplementary Fig. 10g, IFNγ induced both eIF6 and PD-L1, whereas eIF6 silencing blunted IFNγ-mediated PD-L1 upregulation (Supplementary Fig. 10j). Although PD-L1 transcripts were not detected in our Ribo-seq dataset (Supplementary Fig. 8), likely reflecting limited sequencing depth, our polysome profiling (Supplementary Fig. 10k, l) showed reduced polysome association of PD-L1 mRNA and its upstream regulator STAT1 mRNA after eIF6 knockdown, indicating decreased translational efficiency (Supplementary Fig. 10m). CD47 was similarly translationally downregulated, while HLA-A translation increased, suggesting selective translational control of immune-evasion factors. Accordingly, eIF6 depletion in vivo delayed tumour progression only in immunocompetent, not nude, mice (Supplementary Fig. 10n), supporting a lymphocyte-associated immune-dependent role for eIF6 in SCLC. Together, these findings suggest a reciprocal interplay between eIF6-mediated translational control and immune-microenvironmental adaptation that may be involved in non-NE transdifferentiation and tumour immune evasion in SCLC, warranting further investigation in an immune-competent context.

eIF6 moonlighting integrin-FAK complex assembly in non-NE SCLC

Given that eIF6 knockdown does not directly affect the translation of known regulators of SCLC transdifferentiation, we next sought to understand how elevated eIF6 expression contributes to the non-NE transition in SCLC. To study this intrinsic role of eIF6 in SCLC neuroendocrine plasticity, we first established an in vitro eIF6-ribosome binding assay using sucrose gradient ultracentrifugation[19]. Cell lysates were subjected to sucrose gradient sedimentation, which allowed the separation of ribosome-associated and free eIF6. Specifically, 60S subunit-bound eIF6 pelleted in fraction F2 through a 30% sucrose cushion, whereas ribosome-free eIF6 remained in fraction F1(Fig. 5a, top). Immunoblot analysis revealed a reduced abundance of eIF6 in the F2 fraction of non-NE H69M cells compared to their NE counterparts (H69) (Fig. 5a, bottom). Further analysis of eIF6 distribution within polysome profiles showed diminished eIF6 levels in monosome-associated fractions of non-NE cells (Supplementary Fig. 11a). These findings suggest that in the non-NE cell state, eIF6 undergoes dissociation from the ribosome pool, potentially altering its regulatory function in translation.

We next leveraged large-scale CRISPR screening data from the Cancer DepMap dataset to search for potential pathways that may be associated with eIF6 expression across ~1200 solid cancer cell lines[44]. We performed linear regression analyses to assess the correlation coefficient between eIF6 expression and gene dependency scores for each perturbed gene, identifying genes with the most negative correlation coefficients as those essential for the survival of eIF6-high tumour cells (**Methods**). Consistent with its role in ribosome biogenesis, eIF6-high tumour cells exhibited increased dependency on 60S ribosome assembly factors, including *SBDS* and *EFL1*, two main eIF6 interactors (Fig. 5b and Supplementary Data 5). Unexpectedly, components of two additional pathways – Hippo-YAP pathway and the integrin-FAK signal complex – emerged as essential for eIF6-high tumour cell survival (Fig. 5b and Supplementary Data 5). In contrast, the lysine demethylase EZH2, whose inhibition promotes non-NE transdifferentiation[45], displayed a positive correlation with eIF6 expression, suggesting a potential opposing role in lineage plasticity. We were particularly intrigued by the integrin-FAK pathway, given its established role in EMT across various contexts and the lack of prior studies linking eIF6 to its regulation in SCLC. To further explore this relationship, we analysed the eIF6 genome-wide interactome using the BioGrid database[46], revealing an interaction between eIF6 and integrin β4 protein (ITGB4, also called CD104) (Fig. 5c). Notably, previous studies demonstrated eIF6 binding to CD104 in a yeast two-hybrid assay[47], as well as its ability to localize to intermediate filaments and nuclear matrix[48]. Accordingly, CD104 expression was significantly upregulated in non-NE cell state (Fig. 5d). These lines of evidences suggest a non-classical role for eIF6, wherein it dissociates from ribosomes and associates with the CD104-FAK signalling complex in non-NE SCLC cells.

To investigate whether eIF6 interacts with the CD104-FAK complex, we employed two complementary approaches, including immunoprecipitation and in situ proximity detection. Immunoprecipitation of endogenous FAK revealed an increased interaction between CD104 and FAK in ASCL1-negative non-NE H69M cells compared to ASCL1-positive NE H69 cells (Fig. 5e). Notably, ribosome-dissociated eIF6 also exhibited enhanced interaction with the CD104-FAK complex, coinciding with an increase in phosphorylated ERK1/2 within this complex. These findings suggest that integrin-FAK complex formation is elevated in the non-NE cell state and may activate downstream MAPK signalling (Fig. 5e). We also found increased total CD104 protein levels, aligning with its elevated mRNA expression detected by qPCR (Fig. 5d, 5e). To further validate these interactions in situ, we performed a proximity ligation assay (PLA) followed by our *in-house* PLA analysis pipeline[49] (Fig. 5f). PLA consistently detected eIF6 in close proximity to FAK (Fig. 5g) and CD104 (Supplementary Fig. 11b), with a significant increase in FAK-eIF6 PLA complexes in H69M cells compared to H69 cells (Fig. 5h). Moreover, eIF6 knockdown substantially reduced the number of FAK-eIF6 PLA complexes (Fig. 5g, h) a trend similarly observed in CD104-eIF6 PLA complexes (Fig. 5i and Supplementary Fig 11b). This in situ observation was further corroborated by endogenous FAK immunoprecipitation, which showed that eIF6 knockdown in non-NE H69M cells led to a decrease in total CD104 levels, thereby reducing CD104-FAK complex formation and ERK1/2 association (Fig. 5j).

Previous studies reported that Ser235 phosphorylation by the RACK1–PKCβII complex promotes eIF6 release from the 60S ribosome in other systems[33]. We similarly observed increased Ser235 phosphorylation of eIF6 during non-NE transition across multiple models (Supplementary Fig. 11c). Structurally, eIF6 adopts a characteristic "pentein" fold composed of five α/β subdomains arranged around a pseudosymmetry axis[50], with a C-terminal tail harbouring several phosphorylation sites, including Ser235[51] (Supplementary Fig. 11d). Although we did not directly assess its function, this finding may provide a mechanistic clue for future investigation into whether Ser235 phosphorylation contributes to eIF6 dissociation during non-NE transdifferentiation. Given that such dissociation could expose eIF6 surfaces for alternative binding partners, we next used *AlphaFold3* modelling[52] to explore potential structural interfaces mediating its interaction with the CD104–FAK complex. The modelling suggested that the Calx-β domain of CD104, known to interact with the FAK linker region[53] (Supplementary Fig. 11e), may engage the same surface of eIF6 that associates with the RPL23 (Supplementary Fig. 11f, g). Four residues, Arg57, Ser102, Ser150, and Asp209, were predicted to mediate this interaction, with Arg57 shared by both the RPL23 and CD104 interfaces. The other three residues lie in close proximity to ribosome-interacting residues (Asn106, Tyr151, Glu12, and Ser190)[54] and to Arg61, a residue essential for maintaining eIF6 folding[55](Supplementary Fig. 11h). This spatial arrangement suggests potential competition between CD104 and RPL23 for eIF6 binding. We tried to generate alanine substitutions at these sites, but the mutations resulted in protein misfolding, likely because the mutations disrupted local interactions near Arg61 that are critical for eIF6 structural stability[55], precluding further functional evaluation. Nevertheless, our in silico analyses and validation experiments suggest that eIF6 may exert a moonlighting function by dissociating from ribosomes and associating with the integrin-FAK complex, possibly modulating integrin-mediated downstream signalling in the non-NE cell state.

Targeting integrin-FAK signalling in chemoresistant non-NE SCLC

Following integrin-FAK complex formation, we observed increased focal adhesion kinase (FAK) phosphorylation across multiple SCLC transdifferentiation models (Fig. 6a), as well as upon carboplatin/etoposide treatment (Supplementary Fig. 12a). Transcriptomic analysis revealed a consistent reduction of the MAPK pathway gene signature upon eIF6 knockdown across multiple SCLC models (Fig. 6b, c and Supplementary Fig. 12b), including downregulation of the core MAPK-responsive genes such as *DUSP3, DUSP5, DUSP6* and *MAP2K1* (Fig. 6b). Concordantly, eIF6 knockdown selectively reduced ERK1/2 phosphorylation in the non-NE state, with a similar, albeit less pronounced, effect on FAK autophosphorylation in ASCL1$^+$ H69 and ASCL1$^+$MYCL$^+$ H209 cells (Fig. 6d). Interestingly, a recent study also demonstrated eIF6's interaction with FAK for the local activation of ERK1/2 at focal adhesions in endothelial cells responding to mechanical forces[56]. By contrast, we did not observe measurable changes in AKT phosphorylation (Fig. 6d), in line with our earlier observation that the AKT pathway is not activated during non-NE transition (Supplementary Fig. 2b). To further elucidate the relevance of eIF6 to FAK-ERK

https://doi.org/10.1038/s41467-026-69899-8

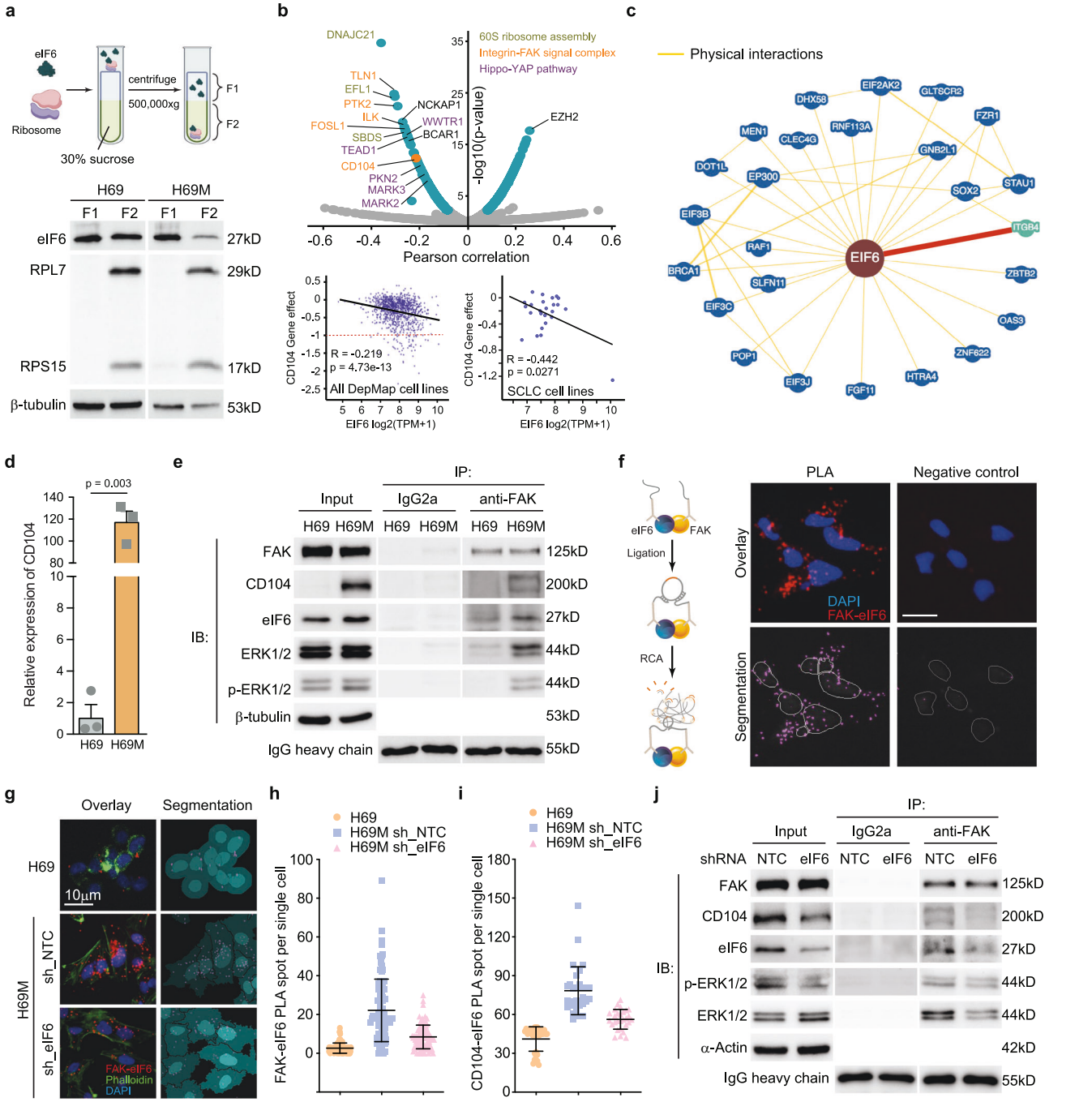

Fig. 5 | eIF6 interacts with the CD104-FAK complex in non-NE cell states. **a** Ribosome binding assay assessing eIF6 association with ribosome pools. Cytoplasmic lysates were fractionated into free (F1) and ribosome-associated (F2) portions via 30% sucrose cushion ultracentrifugation. Immunoblots of eIF6, RPL7, RPS15 and β-tubulin are shown. Representative of two biologically independent experiments were performed with similar results. Created in BioRender. Shen, S. (2026) https://BioRender.com/5p1ea8h. **b** Volcano plot of Pearson correlations between eIF6 expression and gene essentiality across ~1100 solid cancer lines from DepMap. Representative correlations for CD104 are shown for all solid tumours and SCLC lines. Two-sided *p*-values were computed. **c** Direct interaction network of eIF6 from BioGRID. **d** RT-qPCR of CD104 in indicated lines ($n = 3$ biological replicates). Statistical significance: two-sided unpaired Wilcoxon rank-sum test. **e** Co-IP with anti-FAK showing interactions between CD104, eIF6, ERK1/2, and FAK in non-NE states. IgG2a as Co-IP control; β-tubulin and IgG heavy chain for input and IP loading controls. The samples derive from the same experiment, but different gels for FAK, CD104, IgG and β-tubulin, another for p-ERK, ERK and eIF6 were processed in parallel. Similar results were observed in $n = 3$ biologically independent experiments. PLA using anti-FAK and anti-eIF6 (**f**) or anti-CD104 (**g**) antibodies. Red fluorescent signals indicate complexes; scale bars, 10 μm. Protocol validated in three biologically independent experiments. Cell segmentation and spot quantification by CellProfiler. Created in BioRender. Shen, S. (2026) https://BioRender.com/5p1ea8h. Single-cell quantification of eIF6-FAK (**h**) and eIF6-CD104 (**i**) PLA after eIF6 knockdown. Each dot represents a single cell from one representative experiment; two additional biologically independent experiments showed similar trends. **h**: 490 (H69), 197 (H69M sh_NTC), 185 (H69M sh_eIF6); **i**: 472 (H69), 291 (H69M sh_NTC), 210 (H69M sh_eIF6). Two-sided unpaired Wilcoxon rank-sum test. **j** Co-IP of CD104-FAK in H69M cells with eIF6 knockdown. β-tubulin and IgG heavy chain as input/IP loading controls. The samples derive from the same experiment, but different gels for FAK, CD104, IgG, another for p-ERK, ERK, eIF6 and actin were processed in parallel. Similar results were observed in $n = 3$ biologically independent experiments.

https://doi.org/10.1038/s41467-026-69899-8

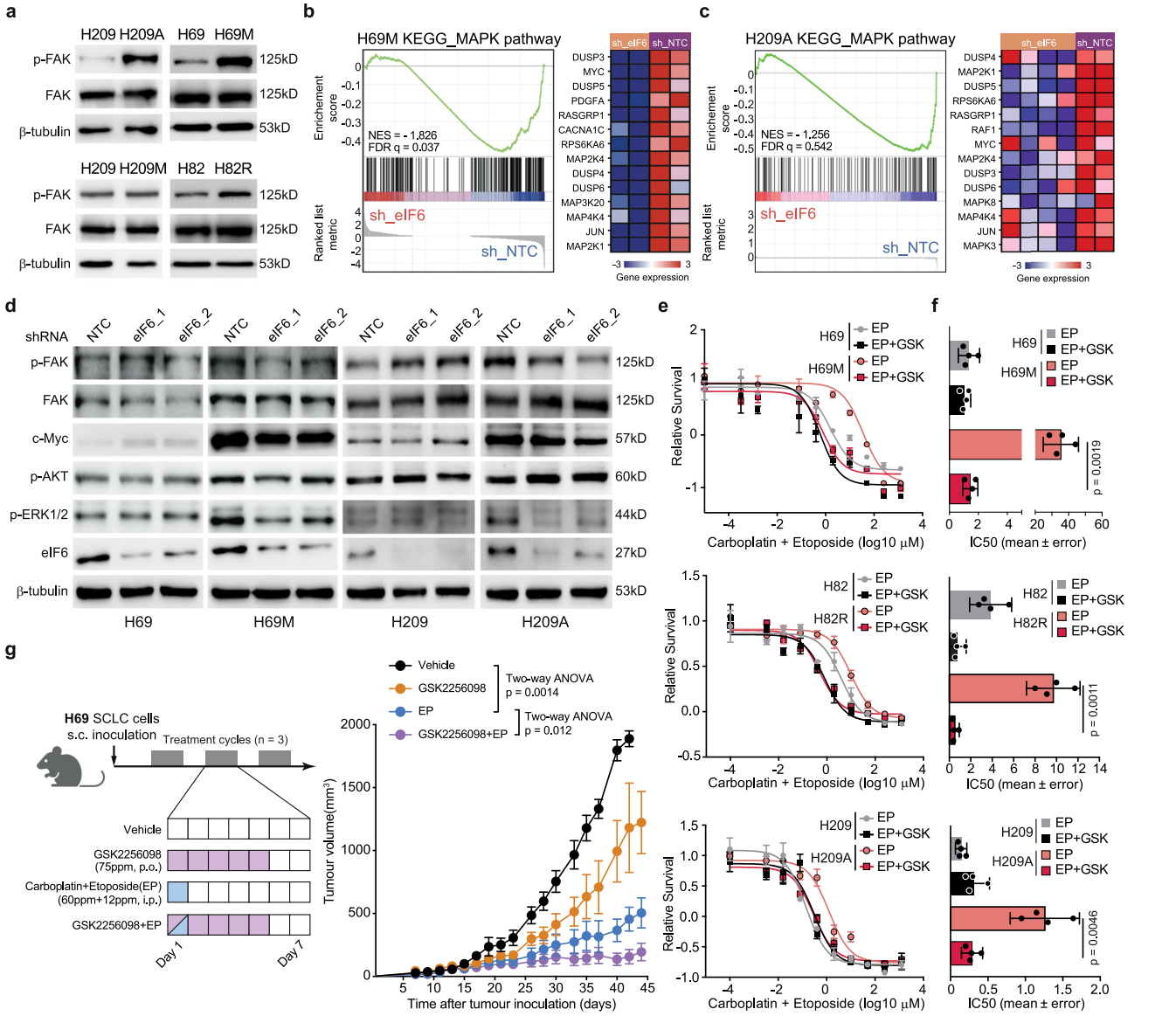

Fig. 6 | FAK inhibition enhances chemotherapy sensitivity in non-NE SCLC. **a** Immunoblot analysis of FAK phosphorylation status across multiple SCLC cell models. β-tubulin was used as a loading control. For H209/H209A, the samples derive from the same experiment, but different gels for FAK, another for p-FAK and β-tubulin were processed in parallel. For H209/H209M, the samples derive from the same experiment, but different gels for p-FAK, another for FAK and β-tubulin were processed in parallel. For H69 and H82 models, the samples derive from the same experiment, but different gels for p-FAK, another for FAK and β-tubulin were processed in parallel. Blots are representative of $n = 3$ biologically independent experiments. eIF6 knockdown in non-NE cell states leads to MAPK pathway downregulation, with the gene expression profiling showing reduced expression of multiple pathway components. H69M cells, RNA-seq analysis is performed in $n = 2$ biologically independent samples (**b**) and H209A cells, RNA-seq analysis is performed in $n = 2$ and 4 biologically independent samples (**c**). **d** Immunoblot analysis of the gene expression and pathway enrichment findings, demonstrating reduced ERK1/2 phosphorylation upon eIF6 knockdown in H69M and H209A cells. For H69/H69M, the samples derive from the same experiment but different gels for p-FAK, p-ERK, another for FAK, another for p-AKT, another for c-Myc, another for eIF6 and β-tubulin were processed in parallel. For H209/H209A, the samples derive from the same experiment, but different gels for p-FAK, p-ERK and c-Myc, another for eIF6, another for FAK, p-AKT and β-tubulin were processed in parallel. Blots are representative of $n = 3$ biologically independent experiments. **e**. CCK-8 cell survival assay following combination treatment with GSK2256098 (10 μM, GSK) and varying concentrations of carboplatin/etoposide (EP) for 72 h across three different SCLC cell models. The treatment response curve of $n = 4$ biologically independent experiments was shown. **f** Half-maximal inhibitory concentration (IC50) of carboplatin/etoposide (EP) in H69 and H69M cell lines. Statistical significance was assessed using a two-sided unpaired t-test with Welch's correction, $n = 4$ biological replicates. **g** H69 tumour cell xenografts in *Balb/cNj-Foxn1^{nu}/Gpt* mice were randomized into four treatment groups when the tumours are palpable, including Vehicle, GSK2256098 monotherapy (75ppm, p.o per day), EP chemotherapy (carboplatin 60ppm + etoposide 12ppm, i.p. per week), and triple therapy (GSK2256098 + EP) (Left panel); Tumour volume (mm^3) was monitored for ~50 days. Data are presented as mean ± SEM. Statistical significance was determined using one-sided two-way ANOVA. Tumour growth curves were shown for $n = 4$ and 6 independent mice. Source data are provided in Source data file. Created in BioRender. Shen, S. (2026) https://BioRender.com/5p1ea8h.

signalling, we overexpressed eIF6 in H69, H82 and H209 cells. EIF6 overexpression in NE cell states increased ERK1/2 and FAK phosphorylation (Supplementary Fig. 12c), consistent with our earlier observation that overexpressing eIF6 in NE cell states enhances HGF-induced non-NE transdifferentiation (Supplementary Fig. 9d–f). Conversely, eIF6 knockdown attenuated ERK1/2 phosphorylation following acute HGF treatment, a known inducer of non-NE transdifferentiation in SCLC (Supplementary Fig. 12d).

Since eIF6 lacks targeted inhibitors and FAK inhibitors are clinically advanced, we tested whether FAK inhibition could sensitize refractory non-NE SCLC to platinum chemotherapy. As a proof-of-concept, we performed drug sensitivity assays in NE and non-NE cells, confirming that non-NE cells exhibit greater resistance to carboplatin/etoposide treatment (Fig. 6e). However, co-treatment with GSK2256098, an effective FAK inhibitor (Supplementary Fig. 12e), restored non-NE cell's sensitivity to chemotherapy, reducing the IC50 values to levels comparable to NE cells in different models (Fig. 6e and 6f). A similar effect was observed with another clinical FAK inhibitor, Ifebemtinib (Supplementary Fig. 12f). In contrast, direct inhibition of ERK1/2 phosphorylation using SCH772984 failed to replicate this effect (Supplementary Fig. 12g). Additionally, MEK inhibition with cobimetinib only partially reduced ERK1/2 phosphorylation in H69M cells (Supplementary Fig. 12h), suggesting that MEK is not the sole upstream regulator in this context, which may explain the limited efficacy of MAPK pathway inhibition alone. Finally, we evaluated the in vivo efficacy of combining FAK inhibition with frontline chemotherapy in H69 xenografts. Mice bearing H69 tumours were treated with GSK2256098, carboplatin/etoposide (EP), or the combination for three cycles (daily GSK2256098 for 5 days and a single EP injection on day 1 of each cycle) (Fig. 6g, left). While either FAK inhibition or EP alone reduced tumour burden, the combination produced the strongest suppression of tumour growth, consistent with our in vitro findings (Fig. 6g, right). Although additional studies in immunocompetent models are warranted, these results highlight the therapeutic potential of pairing FAK inhibitors with platinum-based chemotherapy to counteract SCLC neuroendocrine plasticity and resistance.

Clinical relevance of eIF6 moonlight function in therapeutic response

To evaluate the clinical relevance of our findings for prognosticating SCLC treatment outcomes and identifying patients who may benefit from combined FAK inhibitor and chemotherapy treatment, we collected FFPE tumour samples from a cohort of patients (n = 38) with limited-stage SCLC prior to adjuvant therapies (Supplementary Data 6). Utilizing the proximity ligation assay, we aimed to detect the in situ interaction of CD104-eIF6 or FAK-eIF6 complexes in patient samples (Fig. 7a). Concurrently, we performed mIF staining of eIF6, ASCL1 and NEUROD1 on consecutive FFPE slides, revealing a heterogeneity of CD104-eIF6 or FAK-eIF6 localization dependent on the expression patterns of eIF6 and ASCL1 within the same patient tumour (Fig. 7b and Supplementary Fig. 13a). Notably, CD104-eIF6 spots were scarcely detected in ASCL1-high regions (Figs. 7b, 1), whereas an increased abundance of CD104-eIF6 spots was observed in eIF6-high/ASCL1-low regions (Figs. 7b, 2, 3). Despite a mild correlation between eIF6 expression and NEUROD1 expression, and an inverse correlation with ASCL1 expression within the sample patient samples, no associations were identified between eIF6 expression and tumour stages or metastatic features in this cohort (Fig. 7c). In contrast, the percentage of CD104-eIF6 PLA-positive cells displayed a negative correlation with the percentage of ASCL1-positive cells and a positive correlation with the percentage of eIF6-positive cells (Fig. 7d). These clinical findings substantiate and extend our observations from in vitro experiments and mouse models.

To quantitatively assess eIF6 PLA spots in patient samples, we devised an image-based analysis pipeline (Supplementary Fig. 13b). Initially, we estimated the Hematoxylin-DAB (H-DAB) staining vector by using QuPath and subsequently implemented a script-based cell and spot segmentation approach. This methodology facilitated the identification of PLA spots at the single-cell level (Fig. 7e and Supplementary Fig. 13b). The utilization of such a digital image analysis aimed to mitigate the subjective limitations inherent in visual semi-quantitative scoring methods, providing an adequate dynamic range to represent biomarker expression in our analysis. In this context, we developed an H-score^{PLA} algorithm wherein individual cells and their sub-cellular CD104-eIF6 or FAK-eIF6 spots were detected. PLA-positive cells were then classified into high (3+), medium (2+), or low (1+) based on our pipeline (Fig. 7f and Supplementary Fig. 13b). To comprehensively account for the heterogeneity within an SCLC sample, we randomly quantified at least six different regions on the FFPE slide, and each sample's H-score^{PLA} was calculated (Fig. 7f).

Globally, the percentage of eIF6-positive cells exhibited a mild anti-correlation with event-free survival (EFS), while the opposite trend was observed for the percentage of ASCL1-positive cells (Supplementary Fig. 13c). The H-score^{PLA} of both CD104-eIF6 and FAK-eIF6 strongly anti-correlated with EFS, indicating poorer clinical outcomes when eIF6 functions in a non-classical manner in SCLC (Supplementary Fig. 13c). A multivariate linear regression was conducted to evaluate the relationship between EFS and the explanatory variables, including age, the percentage of ASCL1-positive cells (ASCL1%), the percentage of eIF6-positive cells (eIF6%), and H-score^{PLA} of CD104-eIF6 or FAK-eIF6. In multivariate COX analysis, the higher H-score^{PLA} of CD104-eIF6 and FAK-eIF6 was associated with a lower value of EFS, with an odds ratio of -1.59 (95% CI, -1.895, -1.298) for CD104-eIF6 identified as the most significant biomarker in this cohort (Supplementary Fig. 13d). No significant prognostic value was found for variables such as age, ASCL1% and eIF6%. Furthermore, we did not observe tumour stage dependency of H-score^{PLA} (Fig. 7g). Notably, H-score^{PLA} of CD104-eIF6 exhibited markedly distinct outcomes at a cut-off value of 15 (Fig. 7h, i). Patients with H-score^{PLA} of CD104-eIF6 over 15 demonstrated nearly triple the median EFS compared to those below this threshold (13 months vs. 5.5 months, $p < 0.0001$) (Fig. 7h). Similarly, patients showed a doubling of median overall survival (OS) when their H-score^{PLA} of CD104-eIF6 surpassed 15 (31.93 months vs 15.4 months, $p = 0.0007$) (Fig. 7i). In total, leveraging our H-score^{PLA} algorithm based on the in situ detection of eIF6's non-classical function, we identified distinct SCLC patient subgroups with significant clinical outcomes.

Discussion

We uncovered a potential non-canonical role of eIF6 in SCLC transdifferentiation and neuroendocrine plasticity. In both a GEMM model and limited-stage patient samples, eIF6 expression shows an inverse correlation with ASCL1. In non-NE SCLC cells, eIF6 appears to dissociate from the 60S ribosomal subunit, accompanied by reduced global translation, and associates with CD104, contributing to the CD104/FAK-MAPK signalling. Although eIF6 expression alone shows only a modest correlation with clinical outcomes, our PLA-based scoring of eIF6-CD104 interactions correlates strongly with prognosis. Functionally, eIF6 knockdown delays non-NE transdifferentiation and enhances chemotherapy sensitivity.

EIF6 contributes to the pathogenesis of multiple cancers and ribosomopathies, including paediatric T-cell acute lymphoblastic leukaemia and Shwachman-Diamond syndrome[57]. Its overexpression in colon, ovarian, breast, and liver cancers correlates with poor prognosis, yet its role in drug resistance remains incompletely understood. As a regulator of ribosome biogenesis and translation, eIF6 cooperates with SBDS and EFL1 to control 60S subunit dynamics and maintain proteostasis[17], and *EIF6* haploinsufficiency suppresses transformation driven by dominant-negative *p53/H-RasV12* or *Myc/H-RasV12* in mouse embryonic fibroblasts[18]. Our findings unexpectedly revealed that eIF6 can associate with either ribosomes or the integrin complex, depending on the SCLC cell state. In non-NE cells, eIF6 contributes to CD104-FAK complex assembly, linking translational regulation to cell-ECM signalling. This dual behaviour positions eIF6 as a moonlighting protein, a class of multifunctional factors – spanning metabolic enzymes, transcription and translation factors, and cytoskeletal proteins – whose context-dependent activities are essential for cellular homoeostasis[58]. EIF6 was identified in yeast two-hybrid screens for its interaction with β4 integrin[47] and is enriched in α6β4 integrin-positive

https://doi.org/10.1038/s41467-026-69899-8

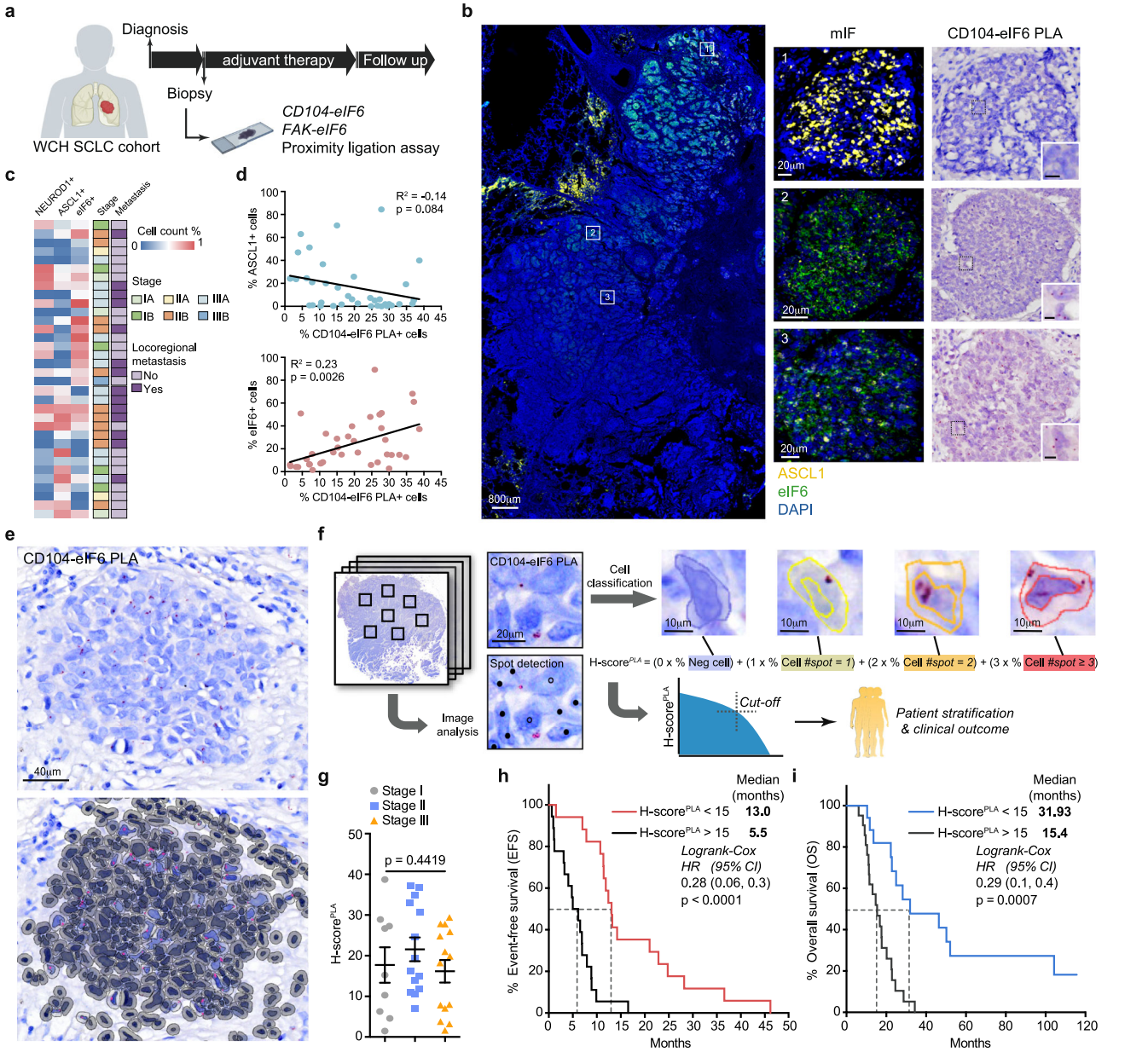

Fig. 7 | In situ detection of eIF6-Integrin/FAK interactions as a prognostic biomarker for SCLC patient outcomes. a Schematic view of patient sample collection. Surgical samples of 38 limited-stage SCLC patients from West China Hospital were used to detect in situ interaction of eIF6-CD104 or eIF6-FAK with proximity ligation assay. Created in BioRender. Shen, S. (2026) https://BioRender.com/5p1ea8h. **b** Representative images of multiplex IF staining for eIF6 and ASCL1 are presented on the left. Scale bars, 800 μm. The magnified view of mIF images and bright field PLA images of CD104-eIF6 interaction within the same area are presented on the right. Multiplex IF and PLA staining were performed on thirty-eight patient samples. Scale bars, 20 μm. For zoom-in images, the scale bars correspond to 10 μm. **c** Quantification of eIF6+, ASCL1+, and NEUROD1+ cells in human SCLC from mIF and their correlation with clinical stages and metastasis status. **d** Correlation between proportion of CD104-eIF6 PLA+ cells and proportion of ASCL1+ cells (top) or eIF6+ cells (bottom). Pearson correlation was calculated using the standard Pearson correlation coefficient. Two-side p values were computed to assess statistical significance. **e** Representative bright field images of PLA detecting CD104-eIF6 interaction (red spot). Segmentation of cells and quantification of red spots at single cell level were conducted in QuPath. PLA quantification was performed on all thirty-eight patient samples, with at least six randomly selected regions of interest per slide. Scale bars, 40 μm. **f** The overview of the workflow demonstrating the PLA image analysis pipeline for patient stratification based on H-score^{PLA}. Created in BioRender. Shen, S. (2026) https://BioRender.com/5p1ea8h. **g** Comparison of CD104-eIF6 H-score^{PLA} across different clinical stages. $n = 9, 15, 14$ patients for stage I, II and III, respectively. Differences among the three groups were assessed using a two-sided one-way ANOVA. Kaplan-Meier survival curves of event-free survival (**h**) and overall survival (**i**) for SCLC patients stratified by H-score^{PLA} of CD104-eIF6 (H-score^{PLA} > 15 groups and H-score^{PLA} < 15 groups). The log-rank *t* test was used for significance analysis. HR hazard ratio, CI confidence interval, ns not significant.

tissues, where it supports hemidesmosome assembly[48]. Like several ribosome-associated proteins that switch functions through post-translational modifications (PTMs)[58,59], exemplified by phosphorylated RPS3 acquiring nuclear roles[60,61], eIF6 also carries multiple phosphorylation sites, including Ser174/175[62] and Ser235[63]. Additional phosphorylation sites, such as Tyr113, Ser239, Ser243, and Ser245, have been identified, but their regulatory kinases and functional consequences remain mostly unknown[57]. We showed that phosphorylation of eIF6 at Ser235 is upregulated across multiple SCLC non-NE transition models. Given that Ser235 phosphorylation promotes eIF6

release from 60S subunits[63], this modification may represent a regulatory axis enabling eIF6 to shift from translational control toward non-canonical interactions in the non-NE state. Using Alphafold-based structural modelling, we explored the potential mechanism of interaction between eIF6 and the integrin complex. Notably, eIF6 residuals predicted to mediate CD104 binding (Ser102, Ser150, Ser19) lie in close proximity to ribosome interacting residuals (Asn106, Tyr151, Glu12, Ser190)[54], and both interfaces appear to converge near Arg57. This spatial convergence raises the possibility that phosphorylation-driven conformational changes may bias eIF6 toward one interaction surface over another, thereby modulating its partitioning between ribosome-bound and integrin-associated states. Although our attempts to express mutant eIF6 containing all four key residues were unsuccessful, likely due to proper structural folding, the in silico observations highlight a mechanistic framework worth testing. Future studies dissecting how individual residual and the associated PTMs influence eIF6's structural dynamics, ribosome affinity, and integrin complex engagement will be essential for defining how eIF6 moonlighting behaviour contributes to SCLC plasticity.

Lineage-based stratification of SCLC (ASCL1, NEUROD1, POU2F3) has highlighted the therapeutic relevance of NE-to-non-NE transitions[6], which frequently couple to EMT-driven metastasis and chemoresistance[64]. Although FAK-mediated EMT is underexplored in SCLC, its established role in other cancers[65] and our in silico link between eIF6 expression and integrin-FAK/Hippo pathway essentiality provide a rationale for targeting this axis. Indeed, FAK and phosphorylated-FAK (Tyr397) are elevated in SCLC versus NSCLC[66], and FAK signalling is broadly upregulated in SCLC lines[67]. Consistent with prior evidence that FAK inhibitor PF573228 induces apoptosis in non-NE-enriched SCLC models[68], we showed that the clinical-grade FAK inhibitor GSK2256098[69] selectively sensitizes non-NE cells to carboplatin/etoposide, providing proof-of-concept for its therapeutic potential in overcoming SCLC resistance. Ongoing clinical evaluation of Ifebemtinib, a FAK inhibitor[70], in combination with anti-PD-L1 and platinum-etoposide (NCT06030258) underscores the translational momentum behind this pathway. In line with these clinical investigations, our preclinical study on eIF6's moonlighting function may help refine biomarker-guided patient selection, though validation in large cohorts remains essential.

Downstream of the integrin-FAK complex, MAPK signalling is a central determinant of proliferation and differentiation[71], and combined FAK-MEK inhibition is already being tested clinically (NCT02428270). Although our findings suggest an eIF6-CD104/FAK axis regulating MAPK activation in non-NE SCLC, direct inhibition of downstream MEK or ERK kinase cannot completely reverse the non-NE transition or sensitize SCLC to chemotherapy, thus other contributors likely intersect. For instance, $KRas^{V12}$ overexpression can drive NE-to-non-NE transition[72], and hyperactive RAS-MEK-ERK signalling suppresses NE identity and NE-SCLC growth[73]. Given that RAS can either activate or suppress integrin signalling in a context-dependent manner[74], dissecting how eIF6 interfaces with FAK and RAS circuitry will be important to understanding SCLC plasticity. Additional pathways may also explain why direct ERK inhibition does not phenocopy FAK blockade. A recent high-throughput screen in uveal melanoma showed that PKC, which phosphorylates eIF6 at Ser235, can drive ERK activation independently of FAK and RAS[75]. Moreover, FAK signalling in eIF6-high tumours may rely on PKN2, a dependency highlighted in our DepMap analysis. Intriguingly, Darovasertib, an FDA-approved therapy for uveal melanoma, can target both FAK-PKN2 and PKC, making it a potential candidate for evaluation in the SCLC setting.

Our study has several limitations that warrant future investigations. First, the clinical analyses, including eIF6 expression and PLA-based biomarkers, were performed in a relatively small patient cohort ($n = 38$) restricted to limited-stage SCLC (LS-SCLC), underscoring the need for validation in larger, independent, prospectively collected cohorts. In addition, our cohort consisted exclusively of East Asian patients, among whom 44.7% of tumours were classified as ASCL1-high, considerably lower than the ~70% ASCL1-positive frequency reported in predominantly Caucasian cohorts[20,76]. Interestingly, a recent study from the National Cancer Centre of China reported a similar ASCL1 positivity of 42.5% in Chinese SCLC patients[77,78], consistent with our observations. These findings raise the possibility that SCLC subtype distribution may vary across ethnic populations, highlighting the need for direct, comparative studies to address potential population-specific differences. Second, the mechanisms driving eIF6 upregulation in the non-NE state remain unresolved. Non-NE cells exhibit low ASCL1 expression, which can activate Wnt signalling in high-grade neuroendocrine lung cancer[79] while suppressing a SOX9-associated non-endodermal stem-like fate in SCLC[80]. ASCL1 strongly binds a canonical E-box motif 5'-CAGCTG-3' that we did not observe in eIF6 promoter regions[81]. Moreover, chemotherapy rapidly increases and maintains eIF6 expression without reducing ASCL1, suggesting that eIF6 is unlikely to be a direct ASCL1 suppressive target. Instead, its inducibility by starvation and IFNγ points toward regulation by extrinsic cues or the integrated stress response (ISR). Whether ISR factors such as ATF4 contribute to eIF6 upregulation remains an important question. A further limitation is that our study largely focuses on cell-intrinsic mechanisms. Because inflammation and the non-NE state are closely linked, the observed enrichment of CD8 + T cells in eIF6-high tumour regions raises the possibility of IFNG-IFNR1 signalling shaping eIF6 expression in vivo. Knockdown of eIF6 reduces PD-L1 and CD47 expression in non-NE cells, primarily through translational mechanisms, suggesting that eIF6 may modulate immune evasion in the inflammatory SCLC context. These observations highlight the need for future work in immunocompetent models to dissect the reciprocal interactions between tumour-expressed eIF6 and the microenvironment during SCLC plasticity.

In summary, our study reveals a regulatory function of eIF6 in SCLC subtype plasticity and chemotherapeutic response. By linking translational control to integrin-FAK signalling, eIF6 serves as an important player in the adaptation of SCLC cells to treatment pressures. These findings provide a strong rationale for targeting eIF6-mediated pathways to improve SCLC therapeutic strategies and patient outcomes.

Methods

Reagents and antibodies

The following chemicals (stored at −20 °C or −80 °C) were used for experiments where indicated: Carboplatin (Selleckchem #S1215, stock 10 mM), Etoposide (Selleckchem #S1225, stock 50 mM in DMSO), Harringtonine (Abcam #ab141941, stock 100 μg ml^{-1} in DMSO), Cycloheximide (MCE, #HY12320, stock 100 mg ml^{-1} in DMSO), GSK-126 (MCE, #HY13470, stock 10 mM in DMSO), ifebemtinib (Selleckchem #E1114, stock 10 mM in DMSO), SCH772984 (Selleckchem #S7101, stock 10 mM in DMSO), GSK2256098 (Selleckchem #S8523, stock 10 mM in DMSO), Cobimetinib (Selleckchem #S8041, Stock 10 mM in DMSO), Rapamycin (Selleckchem #S1039, stock 10 mM in DMSO). The following primary antibodies were used: rabbit anti-RPL7 (Proteintech #14583-1-AP, China, 1:1,000, RRID: AB_2254049), rabbit anti-RPS15 (Proteintech #14957-1-AP, China, 1:1,000, RRID: AB_2180163), rabbit anti-phospho-RPS6 (Ser235/236) (CST #2211S, USA, 1:1,000, RRID: AB_331679), rabbit anti-RPS6 (CST #2217, USA, 1:1,000, RRID: AB_331355), rabbit anti-eIF6 (CST #3263, USA, 1:1,000, RRID: AB_2293295), rabbit anti-phospho-FAK (Tyr397) (CST #8556T, USA, 1:1000, RRID: AB_10891442), mouse anti-FAK (Santa Cruz, #sc-1688, USA, 1:200, RRID:AB_627576), rabbit anti-phospho-AKT (Ser473) (CST #4060, USA, 1:1,000, RRID: AB_2315049), rabbit anti-AKT (CST #9272, USA, 1:1,000, RRID: AB_329827), rabbit anti-phospho-ERK1/2 (CST #4376S, USA, 1:1,000, RRID: AB_331772), rabbit anti-ERK1/2 (CST #9102S, USA, 1:1,000, RRID: AB_330744), rabbit anti-c-Myc (CST #18583, USA, 1:1,000, RRID: AB_2895543), rabbit anti-N-Myc (D4B2Y)

(CST #51705, USA, 1:1,000, RRID: AB_2799400), rabbit anti-L-Myc (E3M5P) (CST #76266T, USA, 1:1000, RRID: AB_2943075), rabbit anti-ASCL1 (E6Y1B) (CST #55467, USA, 1:1,000, RRID: AB_2936422), rabbit anti-NEUROD1 (D90G12) (CST #7019, USA, 1:1,000, RRID: AB_10859914), rabbit anti-YAP1 (CST #14074S, USA, 1:1,000, RRID: AB_2650491), rabbit anti-FAK (Proteintech #12636-1-AP, China, 1:1000, RRID: AB_2173668), rabbit anti-CD104 (Proteintech #21738-1-AP, China, 1:1000, RRID: AB_10733888), rabbit anti-Vimentin (CST #5741, USA, 1:1,000, RRID: AB_10695459), rabbit anti-ZEB1 (CST #3396, USA, 1:1000, RRID: AB_1904164), rabbit anti-ZEB2 (CST #97885, USA, 1:1000, RRID: AB_2934315), rabbit anti-TWIST1 (CST #90445, USA, 1:1000, RRID: AB_3064916), rabbit anti-SNAIL (CST #3879, USA, 1:1000, RRID: AB_2255011), rabbit anti-p70 S6 Kinase (CST #9202, USA, 1:1000, RRID: AB_331676), rabbit anti-phospho-p70 S6 Kinase (Thr389) (108D2) (CST #9234, USA, 1:1000, RRID: AB_2269803), rabbit anti-4E-BP1 (53H11) (CST #9644, USA, 1:1000, RRID: AB_2097841), rabbit anti-phospho-4E-BP1 (Ser65) (CST #9451, USA, 1:1000, RRID: AB_330947), rabbit anti-eIF6 (Proteintech #10291-1-AP, China, 1:100, RRID: AB_2096515), rabbit anti-eIF4A1 (CST #2490, USA, 1:1000, RRID: AB_823487), rabbit anti-eIF4E (CST #2067, USA, 1:1000, RRID: AB_2097675), rabbit anti-PD-L1 (CST #13684, USA, 1:1,000, RRID: AB_2687655), rabbit anti-STAT1 (CST #14994, USA, 1:1,000, RRID: AB_2737027), rabbit anti-Phospho-eIF6 (Ser235) (Thermo Fisher #PA5-6482, USA, 1:1,000, RRID: AB_263008), mouse anti-CD104 (R&D systems #MAB4060, USA, 1:100 from 500 μg ml^{-1} stock, RRID:AB_2296355), rabbit anti-NeuroD1 (Abcam #205300, UK, 1:50, RRID:AB_3083561), Rabbit anti-ASCL1 (BD #556604, USA, 1:100, RRID:AB_396479), mouse anti-POU2F3 (Santa Cruz #sc-293402, USA, 1:500, RRID:AB_2890011), mouse anti-YAP1 (Santa Cruz #sc-101199, USA, 1:1000, RRID:AB_1131430), rabbit anti-CD68 (Abcam #192847, UK, 1:200, RRID:AB_3076701), rabbit anti-CD20 (Invitrogen #PA5-16701, USA, 1:100, RRID:AB_10980806), rabbit anti-CD3 (MXB #MAB-0740, China, ready-to-use antibody), rabbit anti-β-tubulin (ZSGB-BIO #TA-10, China, 1:3000, RRID:AB_3095964), mouse anti-α-actin (ZSGB-BIO #TA-09, China, 1:3000, RRID:AB_2636897).

SCLC genetically engineered mouse model and adenovirus infection

RPM mice bearing deletions of *TP53*, *Rb1*, and amplification of Myc^{T58A} were purchased from The Jackson Laboratory, stock no. 029971. The induction of SCLC tumours in RPM GEMM has been described previously[34]. Briefly, SCLC tumours were induced in RPM mice at 5–7 weeks of age by intranasal instillation with 1×10^8 plaque-forming units of Ad5-CGRP-Cre (University of Iowa). In situ lung tumour tissue was harvested at 4-8 weeks post-adenovirus infection.

Micro computed tomography Imaging

RPM mice were imaged regularly to monitor tumour development from four weeks after adenovirus induction. Mice were anesthetized with isoflurane and imaged by small animal micro computed tomography (microCT) (PINGSENG Healthcare (KunShan) Inc, China, #NMC-100). Cruiser (version 1.6.9.3) software was used for image collection. Mice were scanned using "mouse visceral scanning" protocol with a tube voltage of 60 KV, a tube current of 0.13 mA, and a transverse FOV of 100 mm. Primary images were processed by the Iteration reconstruction algorithm for three-dimensional reconstruction in software Recon (1.6.9.3). The output images with axial, coronal and sagittal planes were visualized and analysed in Avatar (1.6.9.3). When signs of airway thickening or tumour development were shown on microCT images, the RPM mice were sacrificed for further analysis.

Generation of mouse SCLC cell line from RPM GEMM and in vitro cell culture

Once tumour developed and was detected by microCT, RPM mice were sacrificed and the whole lungs were quickly extracted. After washed in ice-cold PBS, the central portion of the mouse lung, including most of the tumour tissue were cut from the lungs and minced several times into small pieces in the enzymatic digestion media with sterile scissors. The digestion cocktail consists of 0.33 U/ml collagenase P (Sigma-Aldrich #11213857001), 0.85 U ml^{-1} Dispase (Sigma-Aldrich #D4693), 144 U ml^{-1} DNase I (Sigma-Aldrich #DN25), 100 U ml^{-1} penicillin and 100 μg ml^{-1} streptomycin in 5 ml Roswell Park Memorial Institute (RPMI) medium without serum. Tissue pieces were then incubated in 2.5 ml digestion media at 37 °C, 5% CO_2 for 1.5-2 hours with periodic pipetting every 30 minutes until well digested. Digestion was stopped by adding the same volume of complete RPMI medium with 10% FBS. The tissue suspension was then filtered through a 70 μm cell strainer (BIOFIL, #CSS013070) and centrifuged for 5 minutes at 2000 rpm. Cell pellets were re-suspended in 3 ml RBC lysis buffer (Thermo Fisher Scientific, #00-4333-57), incubated at room temperature (RT) for 3 minutes, centrifuged at 1000 rpm for 3 minutes, re-suspended in complete RPMI culture medium, and seeded in a T25 cell culture flask (Thermo Fisher Scientific, #156367). After 2a -day culture at 37 °C, 5% CO_2, SCLC tumour cells in suspension were isolated from adherent stromal cells and reseeded in a T25 or T75 culture flask (Thermo Fisher Scientific, #156499) with fresh medium. Following a 2-week culture in vitro, these tumour cells transformed from spherical suspension growth to adherence growth. Early-passage cell lines were cultured for less than 3 weeks, and late-passage cell lines were cultured for more than a month. All RPM GEMM-derived cell lines were validated by immunoblotting for ASCL1 and MYC.

Xenograft and syngeneic mouse model

All experimental mice were maintained in a specific-pathogen-free (SPF) animal centre with regulated environmental conditions. The ambient temperature was kept at 22 ± 2 °C with a relative humidity of 55 ± 10%. An automated 12-hour light/12-hour dark cycle was implemented, and the mice were provided with free access to food and water throughout the study.

To establish human cell-derived xenograft models, 1×10^7 H69, H69 sh_NTC, or H69 sh_eIF6 cells, or 5×10^6 H82 cells were implanted subcutaneously on the right lower quadrant of 6- to 8-week-old female immunocompromised *BALB/cNj-Foxn1^{nu}/Gpt* mice from GemPharmatech (Strain No. D000521). For in vivo experiments of RPM-derived SCLC cells, 1×10^6 RPM-derived mouse SCLC cells with or without eIF6 knockdown were subcutaneously injected into the right lower quadrant of 6- to 8-week-old male C57BL/6JGpt mice from GemPharmatech (Strain No. N000013) or 6- to 8-week-old nude mice as described above. Tumour volume was assessed by an independent, blinded experimenter using a calliper three times per week, and the volume was calculated as follows: $V = (\text{length} \times \text{width}^2)/2$. Based on our animal protocol, the tumours did not exceed 1500 mm^3 in volume. Investigators who performed the drug injection were blinded to the mice group allocation.

Chemotherapy treatment in vivo

Mice bearing H69 or H82 cells were randomized and started on the combination chemotherapy or vehicle when tumour reaching to 400- to 500- mm^3. Mice were treated weekly with carboplatin (60 mg/kg) in PBS and etoposide (12 mg/kg) in 70% PEG300 (MCE, HY-Y0873, USA) in water, or PBS vehicle by intraperitoneal injection (i.p.). Residual tumours were collected at the 3rd week of chemotherapy, while regrowth tumours were harvested when the tumour relapsed and reached 1000 mm^3 after 3 cycles of chemotherapy.

For drug response test on H69 sh_NTC and H69 sh_eIF6 cells xenograft, mice with tumour reaching 100-200 mm^3 were started on 3 weeks of combination chemotherapy as described above. One week after drug withdrawal, mice were sacrificed and the tumours were collected for IHC staining. The endpoint for this in vivo experiment was determined based on tumour volume not exceeding 1500 mm^3.

For combination therapy experiments with the FAK inhibitor GSK2256098 and chemotherapy, mice bearing H69 cells were randomized into four treatment groups when the tumour volume reached 100–200 mm^3: (1) vehicle, 100 µL, oral daily; (2) GSK2256098, 75 mg/kg in 100 µL vehicle, oral daily; (3) carboplatin (60 mg/kg) and etoposide (12 mg/kg), i.p. weekly; (4) a combination of GSK2256098 and chemotherapy at the aforementioned doses and schedules. Three weeks after treatment initiation, the mice were sacrificed, and tumours were harvested for further analysis. All animals were stopped at the endpoint determined by the tumour volumes of the group treated with vehicle reach 1500 mm^3.

Preparation of the mouse subcutaneous tumour for analysis

Mice were sacrificed and tumours were dissociated mechanically with sterile scissors and washed in PBS. For IHC and H&E staining, tumours were fixed in 4% paraformaldehyde (PFA, Beyotime Biotechnology), as explained in detail below. For protein extraction, tumours were minced into small pieces and placed into 2 ml homogenizing CK14 centrifuge tubes (Precellys, France, #P000912-LYSK0) with grinding beads and 300 µl ice-cold RIPA lysis buffer (CST #9806) supplemented with protease inhibitor cocktail (Solarbio, China #P6730) and phosphatase inhibitors (Solarbio, China #P1260). The tissue was then ground by a homogenizer Bioprep-24R (Allsheng, China) for 5 cycles with 30 seconds on and 30 seconds off for each cycle at 4 °C, 4260 rpm. Following grinding, tumours were placed on ice for at least 30 minutes for further lysis and then centrifuged for 10 minutes at 4 °C, 17,000 *g* to dissociate the clear supernatant containing protein.

Human cell lines and cell culture

Human SCLC cell lines NCI-H69 (#HTB-119), NCI-H209 (#HTB-172), NCI-H196 (#CRL-5823), and DMS114 (#CRL-2066) were acquired from the American Type Culture Collection (ATCC). NCI-H82 (#SCSP-5078) and H82R (#SCSP-5097)[25] were purchased from the National Collection of Authenticated Cell Cultures in China. All the above cell lines were authenticated by STR. H69M cell lines were generated in the laboratory from H69 cells and have been described previously[24]. 1×10^6 H69 cells were seeded in 60 mm dishes (NEST, China, #705001) with complete 1640 culture medium containing 40 ng ml^{-1} human recombinant HGF (Peprotech, #100-39H). Fresh medium with HGF was changed every 2 days for 14 days and the adherent cells were isolated and maintained in culture for 1 month. H209M cell lines were generated from H209 cells following the same procedure. A small set of H209 cells that spontaneously adhered to the dish was isolated and maintained in culture for 6 weeks, named H209A. The generated H69M, H209M, and H209A cell lines were confirmed by the morphological changes under light microscopy and immunoblot analysis. All cell lines were incubated at 37 °C with 5% CO_2 in a humidified environment and cultured in RPMI-1640 medium (Gibco #C11875500CP) supplemented with 10% foetal bovine serum (FBS, Lonsera #S711-001S), except for 293 T cells, which were cultured in complete DMEM (Gibco #C11995500CP). All cell lines were subjected to periodic PCR-based testing (SoutherBiotech #13100-01) to confirm their mycoplasma-free status.

SCLC cell transdifferentiation assay

Early-passage mouse SCLC cells were transduced with lentivirus containing eIF6 shRNA (sh_eIF6) or non-targeting control (sh_NTC). 72 hours after infection, mouse SCLC cells of each group were then plated at 1×10^5 per well in six-well plates. Seven days later, cells were stained with crystal violet for visualization. Bright-field images were captured by using a Nikon Eclipse 80i microscope (Nikon, Japan). For human SCLC cells, 1×10^5 H69_shNTC, H69_sh_eIF6 and H69_shrescue cells were seeded per well of a six-well plate in 2.5 ml complete medium containing 40 ng ml^{-1} HGF or 5 µM EZH2 inhibitor (GSK126) on day 1. Culture medium with 40 ng ml^{-1} HGF or 5 µM EZH2 inhibitor was changed every 48 hours. On day 14, representative bright-field images were captured by microscopy. Following twice-washing to remove non-adherent cells, the adherent cells were then stained with crystal violet for quantification of attached colony numbers and area. Similarly, HGF-induced transdifferentiation assays were performed in H69, H82 and H209 cells stably overexpressing eIF6 (pCDH-eIF6) and their corresponding empty vector controls (pCDH-vector), following the same methodology as described above.

Clonal formation assay

RPM-derived mouse SCLC cells were seeded at 1×10^5 cells/well in six-well plates for 24 hours, followed by carboplatin and etoposide or vehicle treatment for 72 hours. Cells were maintained in culture without drugs for another 10 days and then stained with crystal violet for visualizing the entire well and calculating the proportion of colony area in each well.

Cell proliferation and drug sensitivity assay

Cell proliferation and viability were assessed using the CCK8 assay (MCE 2HY-K0301). For the proliferation assay, cells were seeded in 96-well plates at 5×10^3 cells per well and monitored daily for 6 consecutive days. For the drug sensitivity test, cells were seeded in 96-well plates at an initial density of 1×10^4 cells per well and incubated for 24 h before exposure to varying concentrations of carboplatin and etoposide in combination for 72 hours. At indicated time points or at the end of drug treatment, CCK8 was added to the wells at a final concentration of 10%, and absorbance at 450 nm was measured after a 2-hour incubation. IC50 values were determined via nonlinear regression analysis of the dose-response curve, while the growth curve was generated by plotting normalized OD450 nm values against time.

Flow cytometry

H69 and H69M cells were collected, washed twice in PBS, fixed in 4% PFA for 10 minutes at RT, washed in PBS, permeabilized in 0.5% Triton X-100 for 10 minutes at RT, washed in PBS and incubated with rabbit anti-eIF6 antibody (CST 03263, 1:100) in the dark for 15 minutes at RT. Samples were then washed with PBS and incubated with goat anti-rabbit secondary Antibody (Alexa Fluor 488) (Invitrogen 4A-11034) for 30 minutes at RT. After washing, cells were transferred to flow cytometry tubes and analysed on a LSR Fortessa Cell Analyzer (BD). Data analysis was performed with FlowJo (10.8.1) software. For cell viability assay, cells were plated at 1×10^6 cells per well in six-well plates and then treated with CE combined chemotherapy for 72 hours. All cells in each well were collected, washed twice in PBS, and incubated with dead cell stain kit (Invitrogen 8L34966) at 1:500 in the dark for 30 minutes at room temperature. After washing, cells were fixed with 4% PFA for 15 minutes at RT, washed with PBS and transferred to flow cytometry tubes for analysis as described above.

shRNA plasmid

shRNA in the pLKO.1 lentivirus vector targeting specific genes was purchased from Horizon TRC library. The following shRNA target sequences were used for the knockdown experiment: mouse Eif6 (1:TGTCACCACCTGCAATGACTA; 2:GAGAGCGTCTTCAAGCTGAAT), human eIF6 (1: AGAGAACTTCTACAGTGTGTT; 2: ACAGAAGAAATTCTGGCAGAT), and non-targeting shRNA (shNTC, CAACAAGATGAAGAGCACCAA).

Lentivirus production and virus infection

Lentiviruses were made by co-transfection of the shRNA lentivirus vector and the packaging plasmid psPAX2 (addgene#12260) and pMD2.G (addgene#12259) through calcium phosphate co-precipitation into 293 T cells. Virus-containing supernatants were collected at 48 and 72 hours after transfection, filtered through a 0.45 m filter and aliquoted, then frozen at −80 °C. 1×10^6 cells were suspended

in 1 ml lentivirus with 8 μg ml^{-1} polybrene in each well of six-well plates. Virus containing medium was replaced by fresh complete medium 6 hours later. Following 72 hours growth, infected mouse and human SCLC cells were selected in puromycin at 3 μg.ml^{-1} and 1 μg ml^{-1} respectively. The knockdown efficiency was validated by immunoblot after 7–10 days of selection. For the generation of a stable eIF6-overexpression cell line, the lentiviral plasmid heif6-PCDH-NEO (FHDT032) was purchased from Fenghui Biotechnology Company. Lentivirus production and transduction were performed as previously described. 72 hours post-transduction, transduced SCLC cells were selected with 500 μg/mL G418 for two weeks. Successful overexpression of eIF6 was then confirmed by immunoblot.

Polysome profiling

Cells were incubated with 100 μg ml^{-1} cycloheximide for 5 min at 37 °C, washed twice with ice-cold PBS containing 100 μg ml^{-1} cycloheximide, scraped into centrifuge tubes with 5 ml PBS, and centrifugated at 37 °C 300 *g* for 5 minutes. Cell pellets were then lysed in 500 μL hypotonic buffer (5 mM Tris-HCl pH 7.5, 2.5 mM $MgCl_2$, 1.5 mM KCl, 100 μg ml^{-1} cycloheximide, 2 mM DTT, 100 U/ml RNase inhibitor (Promega), 0.5% sodium deoxycholate, 0.5% Triton X-100). The samples were kept on ice for 30 minutes and then centrifuged at 4 °C 17,000 *g* for 10 minutes to remove cell debris. An equivalent amount of ribosomes from each extract was resolved on 5%–60% linear sucrose gradient containing 20 mM HEPES (pH 7.6), 5 mM $MgCl_2$, 100 mM KCl, 100 mg/ml cycloheximide, 100 U/ml RNase inhibitor and centrifuged at 36,000 rpm for 2 hours at 4 °C in a SW40 rotor in an Optima XPN-100 ultracentrifuge (Beckman Coulter, USA). Gradients were fractionated by a Biocomp Gradient Station (BioComp Instruments, Canada) with continuous monitoring of the absorbance at 254 nm. All the polysome plots were processed in MATLAB (Mathworks, USA).

Harringtonine run-off assay

Harringtonine run-off assay had been described[31]. Ribosomes run off the mRNA and the rate of polysome loss was measured using sucrose density gradient centrifugation. In brief, H69 and H69M cells were treated with 2 μg ml^{-1} harringtonine or vehicle at 37 °C for 3 minutes, followed by incubation with 100 μg ml^{-1} cycloheximide for 5 min at 37 °C. Lysates were prepared by scraping the cells into 5 mM Tris-HCl, pH 7.5, 2.5 mM $MgCl_2$, 1.5 mM KCl, 100 μg ml^{-1} cycloheximide, 2 mM DTT, 100 U/ml RNase inhibitor (Promega), 0.5% sodium deoxycholate, 0.5% Triton X-100. An equivalent amount of ribosomes from each extract was resolved on 5–60% linear sucrose gradients for polysome profiling.

Protein extraction from polysome fractions

For immunoblot analysis across polysome fractions in SCLC cell lines, proteins were extracted from the sucrose-containing fractions using the methanol-chloroform precipitation method. Briefly, equivalent volumes of each fraction were mixed with four times the volume of methanol, three times the volume of ultra-pure water and the same volume of chloroform. The mixture was vortexed and centrifuged at 17,000 g for 5 minutes at 4 °C. After centrifugation, the upper aqueous phase was carefully discarded, and one additional volume of methanol was added to the remain. The protein was then precipitated by centrifugation at 17,000 *g* for 15 minutes at 4 °C. The resulting protein pellets were air-dried and resuspended in a consistent volume of lysis buffer, comprising RIPA (CST #9806S) and 4 × Laemmli sample buffer (Bio-red), followed by boiling at 95 °C for 5 minutes. Equal volume of the protein lysates was then subjected to SDS-PAGE and immunoblot analysis.

Ribosome-bound eIF6 assay

H69 and H69M cells were collected and lysed in hypotonic buffer as described above. 800 μl cell lysate of H69 or H69M cells balanced according to total ribosomes were resolved on 1200 μl 30% sucrose cushion containing 20 mM HEPES (pH 7.6), 5 mM $MgCl_2$, 100 mM KCl, 100 mg/ml cycloheximide, 100 U/ml RNase inhibitor and centrifuged at 500,000 *g* (Beckman Coulter, The Optima MAX XP Ultracentrifuge) for 30 minutes at 4 °C in Quick-Seal centrifuge tubes (Beckman Coulter, #344625) in MLA-150 rotor. After centrifugation, 1600 μl of supernatant (F1) and 400 μL of remaining (F2) were collected separately for protein extraction using the methanol-chloroform precipitation method as described above. Equal volumes of the protein lysates from F1 and F2 in H69 and H69M cells were then subjected to SDS-PAGE and immunoblot analysis.

Immunoblotting

Cells were washed twice with ice-cold PBS and lysed in a RIPA lysis buffer (CST #9806S) supplemented with 1 μM DTT, 1 mM PMSF (Solarbio, China #P0100), a protease inhibitor cocktail (Solarbio #P6730) and phosphatase inhibitors (Solarbio, China #P1260). Soluble cell extracts were quantified with Bicinchoninic acid (BCA) assay (Solarbio, China #PC0020) according to manufactories' protocol prior to supplementing with 4 × laemmli sample buffer (Bio-Rad) and boiling for 5 minutes at 95 °C. An equal amount of protein was resolved by 10% SDS gel electrophoresis with Tris/glycine/SDS running buffer, transferred onto nitrocellulose membranes using Tris/glycine transfer buffer, blocked with 5% milk for 1 hour and probed with indicated primary antibodies overnight at 4 °C. Membrane were washed 3 times in PBST, incubated with gout anti-mouse or anti-rabbit horseradish peroxidase-conjugated (HRP) secondary antibodies (ZSGB-BIO #ZB2301, #ZB2305 respectively) at a 1:5,000 dilution in 5% milk for 1 hour at room temperature, washed with PBST for 3 times, then detected with ultra-sensitive ECL chemiluminescence substrate (4 A biotech, #4AW011). Protein was visualized by exposure in a ChemiDoc MP imaging system (Bio-Rad) and quantified with Image Lab (Bio-Rad).

Co-Immunoprecipitation

Cells were washed twice with ice-cold PBS and lysed in IP lysis buffer (50 mM Tris-HCL, 150 mM NaCl, 1% NP40) supplemented with 1 mM PMSF (Solarbio, China #P0100), a protease inhibitor cocktail (Solarbio #P6730) and phosphatase inhibitors (Solarbio, China #P1260). After incubating on a rotator at 4 °C for 1 h, the lysate was centrifuged at 16,000 *g* for 10 minutes to pellet cellular debris. A total of 40 μl lysate was mixed with 10 μl of 5 × loading buffer (Beyotime, #0289) to serve as input protein. The remaining lysate was aliquoted and then added to mouse anti-FAK antibody (Santa Cruz, #sc-1688) or mouse IgG1 isotype control (CST, #5415), respectively. After rotating for 1 hour at room temperature, 30 μl of protein A/G beads (Smart-Lifesciences, #SA-032005) were added, and the mixture was incubated overnight on a rotator at 4 °C. The beads were isolated through centrifugation at 500 *g* for 3 minutes, and then gently washed once with IP lysis buffer, followed by four washes with Wash Buffer (50 mM Tris-HCL, 150 mM NaCl, 0.1% NP40). Residual liquid was removed with fine pipette tips. Beads were then resolved in 30 μl of 1 × loading buffer (4 × sample buffer diluted with RIPA buffer) and boiled at 95 °C for 5 minutes to form IP-lysate. An equal amount of input protein and equal volume of IP-lysate among different conditions were used for immunoblotting.

Tumour secretome analyses

Secretome analyses of H69 and H69M cells were performed by using Proteome Profiler Human XL Cytokine Array Kit (R&D Systems, Inc., USA, #ARY022), per the manufacturer's instructions. Briefly, H69 and H69M cells were seeded in 100 mm dishes at an initial density of 1×10^7 cells and incubated for 48 hours. Cell culture supernatant was collected and centrifuged at 500 *g* for 3 minutes to remove particulates. 500 μl of cell culture supernatant was run on each array per protocol. The membranes were finally scanned using the ChemiDoc MP imaging system (Bio-Rad) and analysed using Image Lab (Bio-Rad).

Quantitative real-time PCR

Total RNA was extracted from cells using TRIzol (Thermo Fisher) according to the manufacturer's protocol and was quantified by Nanodrop microvolume spectrophotometers (Thermo Fisher Scientific). A complementary DNA library was synthesized using Takara PrimeSript RT reagent kit (Takara #RR047A) following the protocol provided by the manufacturer. qPCR was performed using the SYBR Green Supermix (Bio-Rad #1708882) and CFX-96 (Bio-Rad) according to the manufacturer's instructions. Results were normalized to the expression of HPRT1. The primers were synthesized by Youkang Biotechnology Zhejiang Co., Ltd (Hangzhou, China). The following probes were used for qPCR:

Human eIF6 Forward (5′-CCGACCAGGTGCTAGTAGGAA-3′),
Human eIF6 Reverse (5′- CAGAAGGCACACCAGTCATTC-3′),
Human eIF4A1 Forward (5′- CGAAATGTTAAGCCGTGGATTCA-3′),
Human eIF4A1 Reverse (5′- CTCAAGCACATCAGAAGGCAT-3′),
Human eIF4E Forward (5′- TGCGGCTGATCTCCAAGTTTG-3′),
Human eIF4E Reverse (5′- CCCACATAGGCTCAATACCATC-3′),
Human eIF4G Forward (5′- GCCCAGAGCATAGCCCTTC-3′),
Human eIF4G Reverse (5′- GACTGCGAGATTAGGCTCAGA-3′),
Human CD104 Forward (5′-GCAGCTTCCAAATCACAGAGG-3′),
Human CD104 Reverse (5′-CCAGATCATCGGACATGGAGTT-3′),
Human HPRT1 Forward (5′- GGCCAGACTTTGTTGGATTTG-3′),
Human HPRT1 Reverse (5′- TGCGCTCATCTTAGGCTTTGT-3′).

Polysome fraction qPCR

Following polysome profiling, the RNA in monosome fractions and polysome fractions was separately extracted from sucrose using TRIzol LS (ThermoFisher) solution following the manufacturer's protocol. After quantification through Nanodrop microvolume spectrophotometers (ThermoFisher Scientific), the complementary DNA library was synthesized using Takara PrimeSript RT reagent kit (Takara #RR047A). qPCR for immune-related genes and HPRT1 was conducted using the SYBR Green Supermix (Bio-Rad #170882) and CFX-96 (Bio-Rad) according to the manufacturer's protocol. The following probes were used in the experiment:

Human CD274 Forward (5′-GGACAAGCAGTGACCATCAAG-3′),
Human CD274 Reverse (5′-CCCAGAATTACCAAGTGAGTCCT-3′),
Human HLA-A Forward (5′-GATTACATCGCCTTGAACGAGG-3′),
Human HLA-A Reverse (5′-GCAGGGTAGAAGCTCAGGG-3′),
Human STAT1 Forward (5′-ATCAGGCTCAGTCGGGGAATA-3′),
Human STAT1 Reverse (5′-TGGTCTCGTGTTCTCTGTTCT-3′),
Human CD47 Forward (5′-TCCGGTGGTATGGATGAGAAA-3′),
Human CD47 Reverse (5′-ACCAAGGCCAGTAGCATTCTT-3′),
Human HPRT1 Forward (5′-GGCCAGACTTTGTTGGATTTG-3′),
Human HPRT1 Reverse (5′-TGCGCTCATCTTAGGCTTTGT-3′).

Immunohistochemistry and multiplexed immunofluorescence

The tissue was fixed in 4% paraformaldehyde (PFA, Beyotime Biotechnology) for 6-16 hours at room temperature, washed in PBS, transferred to 75% ethanol, and embedded in paraffin within 1 week after surgical resection. 4 μm Formalin-fixed paraffin embedded (FFPE) sections were dewaxed and rehydrated followed by antigen retrieval with EDTA buffer (pH 9.0, ZSGB-BIO #ZLI9069) at 100 °C for 20 minutes. For IHC, slides were quenched with hydrogen peroxide for 10 minutes and blocked with goat serum (ZSGB-BIO #ZLI9056) for 30 minutes at RT. Slides were then incubated with mouse anti-ASCL1 (BD #556604, 1:100), rabbit anti- NeuroD1 (Abcam #205300, 1:50), mouse anti-POU2F3 (Santa Cruz #sc-293402, 1:500), mouse anti-Yap (Santa Cruz #sc-101199, 1:1000) or rabbit anti-eIF6 (CST #3263, 1:100) overnight at 4 °C, washed three times, and incubated with gout anti-rabbit (ZSGB-BIO #PV-6000) for 40 minutes at RT. DAB (CST) was used for staining immunocomplex and hematoxylin was used for counterstaining. For multiplexed immunofluorescence (mIF), Opal Polaris 7-Colour Automation IHC kit (Akoya) was used according to manufacturer's instructions. The following primary antibodies were used for mIF: rabbit anti-eIF6 (CST #3263, 1:50), rabbit anti-NeuroD1 (Abcam #205300, 1:50), mouse anti-ASCL1 (BD #556604, 1:100), rabbit anti-CD68 (Abcam #192847, 1:200), rabbit anti-CD20 (Invitrogen #PA5-16701, 1:100), rabbit anti-CD3 (MXB #MAB-0740, ready-to-use antibody). Bright filed images of IHC and H&E were captured by VS200 whole slide scanner (Olympus LS). mIF slides were imaged using Vectra Polaris imaging system (Akoya). Tumour area of each slide was delineated by a trained pathologist in a blinded fashion. All analyses were carried out using QuPath (v 0.4.3). Each cell was firstly identified, then the positively stained cells within tumour area were quantified for calculating the proportion of ASCL1+, NeuroD1 + , and eIF6+ cells.

Proximity ligation assay

For immunofluorescence PLA of SCLC cell lines, 1×10^5 H69, H69M_shNTC or H69M_sh700 cells were fixed on cell culture slides with 4% PFA for 10 minutes at RT separately. Cells were then permeabilized in 0.2% PBS-Tween 20 for 10 minutes at RT. Fluorescent PLA on cells was performed using Duolink in situ detection reagent (far red, Sigma-Aldrich, #DUO92008) according to manufacturer's protocol. Briefly, slides were blocked with blocking solution for 30 minutes at RT and incubated with rabbit anti-eIF6 (Proteintech #10291-1-AP, 1:100) and mouse anti-FAK (Santa Cruz #sc1688 1:100) or rabbit anti-eIF6 and mouse anti-CD104 (R&D systems, #MAB4060, 1:100 from 500 μg ml^{-1} stock) at 4 °C overnight. Duolink in situ anti-rabbit minus and anti-mouse plus (Sigma-Aldrich, #DUO92008, DUO92001) were used as secondary antibodies. Then, slides were incubated with ligase in ligation buffer and polymerase in amplification buffer sequentially. Cells were stained with phalloidin (FITC, ABclone #RM02836, 1:1,000 in PBS) for 15 minutes at RT prior to mounting with Duolink mounting medium with DAPI (Sigma-Aldrich, #DUO82040). Immunofluorescence images were taken by Nikon Eclipse 80i upright microscope (Nikon) and analysed using CellProfiler (version 4.2.8). Positive PLA signal (red points) was identified and quantified in each cell segmented based on DAPI and phalloidin. For bright-filed PLA, FFPE slides were made and retrieved with EDTA buffer (pH 9.0) following the same protocol in IHC. After blocking, primary antibody incubation, PLA probe incubation, ligation, and amplification (procedure similar to immunofluorescence PLA), slides were incubated with HRP-labelled probe and substrate solution for staining development, followed by counterstaining with hematoxylin (Sigma-Aldrich, #DUO92012). All slides were then imaged by the VS200 whole slide scanner (Olympus LS) and analysed using QuPath (v 0.4.3). Cells with positive PLA signal (red points) were identified and quantified on the single cell level within tumour area for calculating the percentage of CD104-eIF6 positive cells. Tumour cells were then classified into PLA high (3 or more spots within one cell), PLA medium (2 spots within one cell), PLA low (1 spot within one cell) and PLA negative (no spot) cells for calculating H-score^{PLA}.

Patient data

Clinical information and tumour samples of SCLC patients were collected from the Department of Thoracic Surgery and Department of Pathology, West China Hospital (WCH). 85 SCLC patients with enough paraffin-embedded tumour samples for FFPE slides between 2012 and 2020 were first included. Based on the following inclusion and exclusion criteria, 38 patients were finally enroled in our retrospective cohort (Supplementary Data 6). The inclusion criteria: (1) Single lesion; (2) No prior treatment with radiotherapy or chemotherapy; (3) First time undergoing lung surgery; (4) Postoperative pathological diagnosis of SCLC; (5) Availability of regular postoperative follow-up data. The exclusion criteria: (1) Multiple lesions in the lungs; (2) Incomplete clinical information; (3) Prior treatment with radiotherapy or targeted therapy. Event-free survival (EFS) in this study was defined as the length of time that a patient remains free of tumour recurrence,

tumour metastasis or death, confirmed by imaging or biopsy findings after surgery. Overall survival (OS) in this study was defined as the length of time from surgery to a patient's death.

Public Datasets and RNA-seq data analyses

Gene expression data of SCLC patients in this study originated from publicly available clinical SCLC datasets: comprehensive SCLC genomic profiling (GSE69091)[20], Chemotherapy-treatment and tumour relapse cohort (dbGAP with accession #PHS001049, https://www.ncbi.nlm.nih.gov/gap/?term=PHS001049)[9], and IMPower133 cohort dataset (EGAD00001006927, https://ega-archive.org/datasets/EGAD00001006927)[23]. RPM and RPR2 mouse transcriptomic datasets were obtained from GSE89660[34].

Numeric expression values of clinical cases and mouse models are normalized and log2-transformed for further analysis. SCLC gene expression data from the IMPower 133 trial were clustered into NE and non-NE subgroups through the NMF algorithm (NMF R package)[82]. To optimally identify differentially expressed genes, the cluster number was chosen based on the Cophenetic correlation coefficient maximization. Four clusters were eventually selected based on SCLC transcriptomes. ASCL1, NeuroD1, POU2F3, and YAP1 emerged as crucial factors for clustering, and NMF-derived gene signatures are shown in Supplementary Fig. 1a. Upregulated genes in relapsed vs. treatment-naive SCLC patients were used to perform GSEA through GSEA software version 4.1.0. The ranking algorithm was set as signal2noise. Hallmark and GO. BP (version 202302) was chosen as the gene set database. Differential expression of specific genes across SCLC transcript subtypes was performed on count per million (CPM) with GraphPad Prism 9.5.1 in Supplementary Fig. 5c, d. Comparison of gene expression of c-Myc, eIF6 and ASCL1 between RPM and RPR2 tumour was normalized following the description as shown in the corresponding literature[34]. The gene expression correlation of ASCL1 and eIF6 in the IMPower 133 cohort was calculated on transcripts per million (TPM) by Pearson correlation coefficient.

We applied the CIBERSORTx algorithm to deconvolute the bulk RNA-seq data from George et al. and infer the relative fractions of tumour-infiltrating immune cells, with a focus on CD8 +T cells, in SCLC tumour tissues. The analysis, conducted on the CIBERSORTx web portal (https://cibersortx.stanford.edu/), was based on the LM22 signature matrix. Key parameters included 1,000 permutations for significance testing and disabled quantile normalization. Subsequently, the estimated proportions of CD8 + T cells were plotted against eIF6 expression levels. A Wilcoxon rank-sum test, implemented in R software (version 4.0.1), was used to evaluate the statistical significance of the observed differences in groups with various eIF6 expressions.

Polysome profile-based RNA-seq analysis

Following polysome profiling, polysome-bound RNA was extracted from sucrose-containing fractions using TRIzol LS (ThermoFisher) according to the manufacturer's protocol and cytoplasmic RNA was extracted from cell lysate in hypotonic buffer using TRIzol LS as well. RNA concentration and purity were determined using Nanodrop microvolume spectrophotometers (Thermo Fisher Scientific). Polysome-bound RNA and cytoplasmic RNA of each experiment were submitted to Novogene Co., Ltd for the following RNA sequencing. Sequencing libraries were generated using NEBNext Ultra RNA Library Prep Kit for Illumina (NEB, USA, Catalogue #: E7530L) following the manufacturer's recommendations and index codes were added to attribute sequences to each sample. The qualified libraries were pooled and sequenced on Illumina platforms with a PE150 strategy in Novogene Bioinformatics Technology Co., Ltd (Beijing, China), according to effective library concentration and data amount required. Trimmed sequence reads were mapped to GRCh38/hg38 using STAR and count data were generated using HTSeq.

Gene set enrichment analysis of cytoplasmic RNA-seq was implemented by using GSEA software version 4.1.0. GSEA was performed using Hallmark gene sets for epithelial-mesenchymal transition (EMT), TNF-α signalling via NFκB, IL-6-JAK-STAT3 signalling or interferon-α response, neuroendocrine and non-neuroendocrine gene signature[22], 'Top 100 neuroendocrine genes' (Supplementary Data 3)[15] and KEGG_MAPK pathway. Differential gene expression between sh_NTC and sh_eIF6 cells in a specific gene set was normalized by z-score and performed in a heatmap.

Gene expression count was used for paired analysis of cytoplasmic RNA-seq (transcriptome) and polysome RNA-seq (translatome) with R software, which was reported in previous publications[26]. Genome-wide assessment of differential translations with polysome profiling data was calculated with the Xtail package[83]. In brief, Xtail assumes that mRNA abundances in polysomes (actively translated mRNA) are not synchronized with mRNA expressions when a gene is subjected to translational dysregulation under certain experimental or physical conditions. Translation efficiency (TE) of each gene can be calculated by comparing the difference between the log2FoldChange of polysome mRNA and cytoplasmic mRNA. Two independent polysome RNA-seq experiments were performed as biological replicates and were used for the differential analysis using xtail to robustly identify genes with differential translation or transcription. For downstream 5′UTR feature analyses, 5′UTR length and GC content of genes identified by xtail were obtained by matching UCSC hg38 genome annotations using the R package 'biomaRt'. The statistical analyses were conducted after gene identification by xtail and did not involve comparisons across experimental replicates. Accordingly, genes were treated as the units of observation, as 5′UTR length and GC content are intrinsic, gene-specific properties and are independent of experimental replication.

Library preparation for ribosome profiling

Samples were lysed using a specific lysis buffer containing Cycloheximide (50 mg/mL) to arrest ribosomes, and the concentration of the resulting lysate was quantified using Qubit® 2.0 Fluorometer. The cellular or tissue lysates were treated with the non-specific ribonuclease RNase I to digest all RNA except for the ribosome-protected fragments (RPFs). Monosomes were subsequently isolated by size-exclusion chromatography using a MicroSpin S-400 HR Column. RPFs were then purified by PAGE gel purification, selecting fragments corresponding to a size range of 28–32 nucleotides (nt). The ends of the isolated RPFs were phosphorylated, followed by the ligation of 5′-end and 3′-end adaptors. Ribosomal RNA (rRNA) was depleted from the RNA samples using an rRNA depletion kit (Qiagen, cat. 334387). The purified RPFs were reverse-transcribed into cDNA, followed by PCR amplification. The Ribo-seq libraries were constructed using the Multiplex Small RNA Library Prep Set for Illumina (Set1) (NEB, cat. E7300L). The concentration of the final cDNA libraries was measured using a Qubit® 2.0 Fluorometer and adjusted to 1 ng/uL. Library insert size was assessed using an Agilent 2100 Bioanalyzer, and the accurate concentration was confirmed via qPCR. Qualified libraries were pooled and subjected to 50-bp single-end sequencing on an Illumina HiSeq 2000 instrument.

Pre-processing of the ribosome profiling and mRNA-seq data

We used the GRCh38 human genome assembly along with the corresponding Ensembl annotation (release 109), with pre-processing methods and similar parameters as previously described[84,85]. In brief, RNA sequencing raw data were checked for quality control using FastQC, following adapter sequences (AGATCGGAAGAGCACACGTCT) trimming using Cutadapt. For ribosome profiling, ribosome-protected fragments were filtered to retain only reads between 20 and 40 nucleotides, in which low-quality reads were removed if the Phred quality scores were lower than 25, as evaluated using fastx quality filter.

To avoid ribosomal RNA contamination, reads mapped to curated human rRNA sequences were removed using Bowtie 1.1.2. and remaining sequences were then aligned to the genome using STAR with similar parameters as described in previous work[84]. Samtools was used to generate output files, including coordinate-sorted BAM files and transcript-level alignments. Gene-level RNA expression was quantified using HTSeq-count, while the abundance of ribosome-protected fragments was estimated with RiboCode[86,87]. Translation efficiency for each gene was subsequently determined by integrating RNA-seq and ribosome profiling data using xtail[83]. Downstream analyses, including data processing and visualization, were conducted with custom scripts written in Python (v3.11) and R (v4.3.2).

Metagene analyses of ribosome profiling data

Metagene analyses of ribosome profiling data were performed by MetageneAnalysis of RiboMiner[88] with "-u 0 -d 500 -l 100 -n 10 -m 1 -e 5" parameters. Specifically, for genes that exhibited more than one transcript, only the longest transcript was used in all analyses. Only the transcripts with a length of over 100 codons and RPKM more than 10 in the whole CDS region were considered. The ribosome densities were normalized to RPKM.

Tandem mass tag-based mass spectrometry

To quantify and probe the polysome-associated proteins, we used Tandem mass tag (TMT) based Mass spectrometry as described previously[89]. In brief, following polysome profiling via sucrose density gradient centrifugation, fractions of H69 and H69M cells were pooled into three distinct components: monosome (M), light polysome (LP) and heavy polysome (HP). Protein was extracted from these pooled fractions through the methanol-chloroform precipitation method as described above. Two biological replicates were used for each component. Protein pellets were resuspended in dissolving buffer (8 M Urea, 100 mM TEAB, pH 8.5) and underwent 5-minute ultrasound sonication on ice. The dissolved proteins were reduced by 1 M DTT (56 °C, 1 h) before alkylation with iodoacetamide. Protein concentrations were determined by BCA assay (Thermo Fisher Scientific).

For TMT labelling, samples were prepared as previously described[90]. First, they were digested for 4 h at 37 °C in a dissolving buffer containing trypsin. Complete digestion was performed by adding the same concentration of trypsin in combination with $CaCl_2$ for overnight. To make sure the pH value is lower than 3, we have mixed the overnight digested samples with formic acid, followed by centrifugation at 12,000 *g* for 5 min at room temperature. The supernatant was then fractionated on the reverse-phase C18 column, washed three times with washing buffer (0.1% formic acid, 3% acetonitrile) and eluted with elution buffer (0.1% formic acid, 70% acetonitrile). The eluents were stored as lyophilized powders for subsequent TMT labelling and mass spectrometry analysis.

TMT labelling and mass spectrometry were performed at Novogene company (Novogene, China). In brief, 50 µg of each sample was mixed with 100 µL of 0.1 M TEAB buffer and 41 µL acetonitrile-dissolved TMT labelling reagent. 8% ammonia was added after 2 h of TMT labelling buffer incubation to stop the reaction. The lyophilized sample was first dissolved in mobile phase A and clarified by centrifugation at 14,000 × *g* for 20 min at 4 °C. Separation was performed on a C18 column (Waters BEH C18, 4.6 × 250 mm, 5 µm) using a Rigol L3000 HPLC system, with the column temperature maintained at 45 °C. The chromatographic separation employed a binary solvent system consisting of solvent A (2% acetonitrile, pH adjusted to 10.0 with ammonium hydroxide) and solvent B (98% acetonitrile). The eluate was monitored at 214 nm, collected at one-minute intervals, and pooled into ten final fractions. All fractions were subsequently dried under vacuum and reconstituted in 0.1% (v/v) formic acid in water prior to mass spectrometry analysis.

High-resolution peptide profiling was performed using an EASY-nLC™ 1200 UHPLC system coupled to a Q Exactive™ HF-X mass spectrometer (Thermo Fisher, Germany). Peptides were introduced through a Nanospray Flex™ electrospray source, operating at 2.3 kV and 320 °C. Full MS spectra were collected over an m/z range of 350–1500 with 60,000 resolution (m/z 200), an AGC target of 3×10^6, and a maximum injection time of 20 ms. The most abundant precursor ions in each scan were then selected for higher-energy collisional dissociation (HCD) and subsequent MS/MS analysis. Fragment ions were acquired at 45,000 resolution (m/z 200) with an AGC target of 5×10^4, a maximum injection time of 86 ms, and a normalized collision energy of 32%. Only ions exceeding 1.2×10^5 intensity units were subjected to fragmentation, and a dynamic exclusion window of 20 s was applied to prevent repeated analysis of the same precursor.

Analysis of Mass Spectrometry data

The resulting spectra from each run were searched separately against homo_sapiens_uniprot_2022_9_5.fasta.fasta (204961 sequences) database by the search engines: Proteome Discoverer (PD, Thermo, HFX and 480). The searched parameters are set as follows: mass tolerance for precursor ion was 10 ppm and mass tolerance for product ion was 0.02 Da. Carbamidomethyl was specified as fixed modifications, Oxidation of methionine (M) and iTRAQ/TMT plex were specified as dynamic modifications. Acetylation, iTRAQ/TMT plex, Met-loss and Met-loss + Acetyl were specified as N-Terminal modification. A maximum of 2 miscleavage sites were allowed.

In order to improve the quality of analysis results, the software PD further filtered the retrieval results: Peptide Spectrum Matches (PSMs) with a credibility of more than 99% were identified PSMs. The identified protein contains at least 1 unique peptide. The identified PSMs and protein were retained and performed with FDR no more than 1.0%.

Mass spectrometry data from M, LP and HP fractions were grouped together in H69 or H69M cells for principal component analysis (Fig. 2h). All ribosome protein intensity was log2 transformed prior to conducting standard linear regression between H69 and H69M cells in different fractions (M, LP, HP). Linear regressions and Pearson correlations were performed using GraphPad Prism (v 9.5.1).

DepMap-based gene dependency correlation analysis with eIF6 expression

Publicly available CRISPR knockout functional genomics and transcriptomic datasets were obtained from the DepMap 23Q4 release (Broad Institute). Correlation analyses were conducted as previously reported[91] using the DepMap online analysis platform. To assess the relationship between eIF6 expression and genetic dependency, eIF6 transcript levels (TPM) were systematically compared with genome-wide CRISPR knockout dependency scores (Chronos; DepMap Public 23Q4+) across solid tumour-derived cell lines. Two-sided Pearson correlation coefficients were calculated to quantify these associations without multiple-testing correction of p values. In parallel, the same analytical workflow was applied to a restricted subset of small cell lung cancer (SCLC) cell lines, generating SCLC-specific correlations between eIF6 expression and CRISPR dependency scores.

Analysis of public scRNA-seq data

The single-cell RNA-seq data from Chan et al.[42] were obtained via Cell ×Gene [https://cellxgene.cziscience.com/e/34deb33b-a50e-4993-a38b-1c0e5079c1c2.cxg]. The pre-annotated h5ad files were downloaded and processed using Seurat (v.5.1.0). To minimize genetic heterogeneity, only SCLC patients with mutations in both TP53 and RB1 were included. EIF6+ tumour cells were identified as the tumour cell cluster exhibiting the highest EIF6 expression. CD8 + T cells were identified based on the original annotations "effector CD8-positive, alpha-beta T cell" and "CD8-positive, alpha-beta memory T cell". To

investigate potential intercellular crosstalk between tumour subtypes and CD8 + T cells, ligand-receptor distribution and expression were analysed with the R package 'CellChat' (v.1.6.1) following its standard workflow. Secreted autocrine/paracrine signalling interactions were selected for further analysis. The cell-cell communication links were filtered out if they involved fewer than 10 cells in a given interaction. Only statistically significant interactions ($P < 0.05$) were retained.

AlphaFold prediction of eIF6 and CD104 interactions

The potential interaction between human eIF6 and CD104 was predicted using AlphaFold version 3. Structural input files were obtained from the Protein Data Bank (PDB): eIF6 (PDB ID: P56537) and CD104 (PDB ID: 3FQ4). The AlphaFold v3 multimer pipeline was applied to model the heteromeric complex. All parameters were kept at their default settings. Multiple sequence alignments (MSAs) for each protein were automatically generated using AlphaFold's built-in sequence databases, including Uniref90, MGnify, and BFD, to maximize evolutionary information. Structural recycling was performed according to the default number of cycles, allowing iterative refinement of interchain interactions. No custom templates, restraints, or manually defined interfaces were applied. For each complex prediction, five models were generated and ranked by the predicted Local Distance Difference Test (pLDDT) confidence scores and Predicted Aligned Error (PAE) metrics. The top-ranked model was selected for further analysis. Predicted structures were visualized using molecular graphics software to identify potential interaction surfaces, hydrogen bonding, and steric complementarity between eIF6 and CD104. Interface regions were further inspected to assess the plausibility of binding and to highlight key residues potentially mediating the interaction.

Statistics and reproducibility

At least three biological replicates were performed for in vitro/ex vivo assays. For animal experiments, at least 5 mice were used in each conditioned group. No statistical method was used to predetermine sample size. Sample sizes were strategically selected based on previous experience and published literature to ensure the reliability and reproducibility of the observed effects. Mice were inoculated with the indicated tumour cell lines. Prior to treatment initiation, animals were randomized into experimental groups, and tumour measurements were performed by an investigator blinded to treatment allocation. No data were excluded from the analyses. For cell culture experiments, blinding was not possible. For animal experiments, mice were randomized into different groups prior to treatment initiation and investigators who performed drug injection were blinded to the mice group allocation. For RNA-seq and TMT, the investigator who processed and sequenced the samples (Novogene, China) was blinded to the identity of the samples.

Statistical analysis was carried out by using GraphPad Prism (v 9.5.1). Data are presented as mean ± SEM. All pairwise comparisons were assessed by a two-sided unpaired Wilcoxon rank-sum test. The statistical significance of differences among multiple groups was assessed using two-sided one-way ANOVA. Log-rank test and multivariate linear regression were used for analyzing patients' survival data. P values < 0.05 were considered significant.

Ethic statements

All experiment in this study complies with ethical regulations. Animal experiments were performed following the protocol (#20220107014) approved by the Animal Ethics Committee of West China Hospital, Sichuan University. The use of clinical specimens and data (including reporting and sharing individual-level data) in this study was approved by West China Hospital Sichuan University Biomedical Research Ethics Committee (#2022-36), and written informed consent of all patients was obtained.

Reporting summary

Further information on research design is available in the Nature Portfolio Reporting Summary linked to this article.

Data availability

The RNA-seq data generated in this study have been deposited in the Gene Expression Omnibus under accession code GSE262597. The mass spectrometry proteomics data generated in this study have been deposited in the ProteomeXchange Consortium via the iProX partner repository under identifier PXD051035. The RNA-seq and proteomics data are fully available without restrictions. Processed data and all data supporting the findings of this study are provided in the Supplementary Information. Source data are provided with this paper.

References

1. Megyesfalvi, Z. et al. Clinical insights into small cell lung cancer: Tumor heterogeneity, diagnosis, therapy, and future directions. *CA Cancer J. Clin.* **73**, 620–652 (2023).
2. Rudin, C. M., Brambilla, E., Faivre-Finn, C. & Sage, J. Small-cell lung cancer. *Nat. Rev. Dis. Prim.* **7**, 3 (2021).
3. Horn, L. et al. First-Line Atezolizumab plus Chemotherapy in Extensive-Stage Small-Cell Lung Cancer. *N. Engl. J. Med.* **379**, 2220–2229 (2018).
4. Paz-Ares, L. et al. Durvalumab plus platinum-etoposide versus platinum-etoposide in first-line treatment of extensive-stage small-cell lung cancer (CASPIAN): a randomised, controlled, open-label, phase 3 trial. *Lancet* **394**, 1929–1939 (2019).
5. Tang, X. et al. Metabolism and mRNA translation: a nexus of cancer plasticity. *Trends Cell Biol.* **35**, 562–575 (2025).
6. Redin, E., Quintanal-Villalonga, A. & Rudin, C. M. Small cell lung cancer profiling: an updated synthesis of subtypes, vulnerabilities, and plasticity. *Trends Cancer* **10**, 935–946 (2024).
7. Gardner, E. E. et al. Chemosensitive Relapse In Small Cell Lung Cancer Proceeds Through an EZH2-SLFN11 Axis. *Cancer Cell* **31**, 286–299 (2017).
8. Drapkin, B. J. et al. Genomic anD Functional Fidelity Of Small Cell Lung Cancer Patient-derived Xenografts. *Cancer Discov.* **8**, 600–615 (2018).
9. Wagner, A. H. et al. Recurrent WNT pathway alterations are frequent in relapsed small cell lung cancer. *Nat. Commun.* **9**, 3787 (2018).
10. George, J. et al. Evolutionary trajectories of small cell lung cancer under therapy. *Nature* **627**, 880–889 (2024).
11. Ireland, A. S. et al. MYC Drives Temporal Evolution Of Small Cell Lung Cancer Subtypes By Reprogramming Neuroendocrine Fate. *Cancer Cell* **38**, 60–78 e12 (2020).
12. Nguyen, E. M. et al. Targeting Lysine-Specific Demethylase 1 Rescues Major Histocompatibility Complex Class I Antigen Presentation and Overcomes Programmed Death-Ligand 1 Blockade Resistance in SCLC. *J. Thorac. Oncol.* **17**, 1014–1031 (2022).
13. Oser, M. G. et al. The KDM5A/RBP2 histone demethylase represses NOTCH signaling to sustain neuroendocrine differentiation and promote small cell lung cancer tumorigenesis. *Genes Dev.* **33**, 1718–1738 (2019).
14. Duplaquet, L. et al. KDM6A epigenetically regulates subtype plasticity in small cell lung cancer. *Nat. Cell Biol.* **25**, 1346–1358 (2023).
15. Chen, H. Y. et al. Regulation of neuroendocrine plasticity by the RNA-binding protein ZFP36L1. *Nat. Commun.* **13**, 4998 (2022).
16. Fabbri, L., Chakraborty, A., Robert, C. & Vagner, S. The plasticity of mRNA translation during cancer progression and therapy resistance. *Nat. Rev. Cancer* **21**, 558–577 (2021).
17. Jaako, P. et al. eIF6 rebinding dynamically couples ribosome maturation and translation. *Nat. Commun.* **13**, 1562 (2022).
18. Gandin, V. et al. Eukaryotic initiation factor 6 is rate-limiting in translation, growth and transformation. *Nature* **455**, 684–688 (2008).

19. Finch, A. J. et al. Uncoupling of GTP hydrolysis from eIF6 release on the ribosome causes Shwachman-Diamond syndrome. *Genes Dev.* **25**, 917–929 (2011).
20. George, J. et al. Comprehensive genomic profiles of small cell lung cancer. *Nature* **524**, 47–53 (2015).
21. Barbie, D. A. et al. Systematic RNA interference reveals that oncogenic KRAS-driven cancers require TBK1. *Nature* **462**, 108–112 (2009).
22. Zhang, W. et al. Small cell lung cancer tumors and preclinical models display heterogeneity of neuroendocrine phenotypes. *Transl. Lung Cancer Res* **7**, 32–49 (2018).
23. Gay, C. M. et al. Patterns of transcription factor programs and immune pathway activation define four major subtypes of SCLC with distinct therapeutic vulnerabilities. *Cancer Cell* **39**, 346–360 e347 (2021).
24. Canadas, I. et al. Targeting epithelial-to-mesenchymal transition with Met inhibitors reverts chemoresistance in small cell lung cancer. *Clin. Cancer Res.* **20**, 938–950 (2014).
25. Guo, C. et al. Therapeutic targeting of the mevalonate-geranylgeranyl diphosphate pathway with statins overcomes chemotherapy resistance in small cell lung cancer. *Nat. Cancer* **3**, 614–628 (2022).
26. Shen, S. et al. An epitranscriptomic mechanism underlies selective mRNA translation remodelling in melanoma persister cells. *Nat. Commun.* **10**, 5713 (2019).
27. Bohlen, J., Roiuk, M. & Teleman, A. A. Phosphorylation of ribosomal protein S6 differentially affects mRNA translation based on ORF length. *Nucleic Acids Res.* **49**, 13062–13074 (2021).
28. Leppek, K., Das, R. & Barna, M. Functional 5′ UTR mRNA structures in eukaryotic translation regulation and how to find them. *Nat. Rev. Mol. Cell Biol.* **19**, 158–174 (2018).
29. Advani, V. M. & Ivanov, P. Translational Control under Stress: Reshaping the Translatome. *Bioessays* **41**, e1900009 (2019).
30. Jobava, R. et al. Adaptive translational pausing is a hallmark of the cellular response to severe environmental stress. *Mol. Cell* **81**, 4191–4208.e4198 (2021).
31. Ingolia, N. T., Lareau, L. F. & Weissman, J. S. Ribosome profiling of mouse embryonic stem cells reveals the complexity and dynamics of mammalian proteomes. *Cell* **147**, 789–802 (2011).
32. Genuth, N. R. & Barna, M. The discovery of ribosome heterogeneity and its implications for gene regulation and organismal life. *Mol. Cell* **71**, 364–374 (2018).
33. Ceci, M. et al. Release of eIF6 (p27BBP) from the 60S subunit allows 80S ribosome assembly. *Nature* **426**, 579–584 (2003).
34. Mollaoglu, G. et al. MYC drives progression of small cell lung cancer to a variant neuroendocrine subtype with vulnerability to aurora kinase inhibition. *Cancer Cell* **31**, 270–285 (2017).
35. Bankhead, P. et al. QuPath: Open source software for digital pathology image analysis. *Sci. Rep.* **7**, 16878 (2017).
36. Nabet, B. Y. et al. Immune heterogeneity in small-cell lung cancer and vulnerability to immune checkpoint blockade. *Cancer Cell* **42**, 429-443.e4 (2024).
37. Balanis, N. G. et al. Pan-cancer convergence to a small-cell neuroendocrine phenotype that shares susceptibilities with hematological malignancies. *Cancer Cell* **36**, 17–34.e17 (2019).
38. Canadas, I. et al. Tumor innate immunity primed by specific interferon-stimulated endogenous retroviruses. *Nat. Med.* **24**, 1143–1150 (2018).
39. Hillary, R. F. & FitzGerald, U. A lifetime of stress: ATF6 in development and homeostasis. *J. Biomed. Sci.* **25**, 48 (2018).
40. Mello, C. A. et al. Desmoplastic small round cell tumor: a review of main molecular abnormalities and emerging Therapy. *Cancers* **13**, 498 (2021).
41. Newman, A. M. et al. Determining cell type abundance and expression from bulk tissues with digital cytometry. *Nat. Biotechnol.* **37**, 773–782 (2019).
42. Chan, J. M. et al. Signatures of plasticity, metastasis, and immunosuppression in an atlas of human small cell lung cancer. *Cancer Cell* **39**, 1479–1496.e1418 (2021).
43. Jin, S. et al. Inference and analysis of cell-cell communication using CellChat. *Nat. Commun.* **12**, 1088 (2021).
44. Arafeh, R., Shibue, T., Dempster, J. M., Hahn, W. C. & Vazquez, F. The present and future of the Cancer Dependency Map. *Nat. Rev. Cancer* **25**, 59–73 (2025).
45. Mahadevan, N. R. et al. Intrinsic immunogenicity of small cell lung carcinoma revealed by its cellular plasticity. *Cancer Discov.* **11**, 1952–1969 (2021).
46. Oughtred, R. et al. The BioGRID database: A comprehensive biomedical resource of curated protein, genetic, and chemical interactions. *Protein Sci.* **30**, 187–200 (2021).
47. Biffo, S. et al. Isolation of a novel beta4 integrin-binding protein (p27(BBP)) highly expressed in epithelial cells. *J. Biol. Chem.* **272**, 30314–30321 (1997).
48. Sanvito, F. et al. The beta4 integrin interactor p27(BBP/eIF6) is an essential nuclear matrix protein involved in 60S ribosomal subunit assembly. *J. Cell Biol.* **144**, 823–837 (1999).
49. Shen, S., Girault, I., Malka-Mahieu, H., Robert, C. & Vagner, S. In situ detection of the eIF4F translation initiation complex in mammalian cells and tissues. *STAR Protoc.* **2**, 100621 (2021).
50. Groft, C. M., Beckmann, R., Sali, A. & Burley, S. K. Crystal structures of ribosome anti-association factor IF6. *Nat. Struct. Biol.* **7**, 1156–1164 (2000).
51. Jungers, C. F., Elliff, J. M., Masson-Meyers, D. S., Phiel, C. J. & Origanti, S. Regulation of eukaryotic translation initiation factor 6 dynamics through multisite phosphorylation by GSK3. *J. Biol. Chem.* **295**, 12796–12813 (2020).
52. Abramson, J. et al. Accurate structure prediction of biomolecular interactions with AlphaFold 3. *Nature* **630**, 493–500 (2024).
53. Tai, Y. L. et al. An EGFR/Src-dependent beta4 integrin/FAK complex contributes to malignancy of breast cancer. *Sci. Rep.* **5**, 16408 (2015).
54. Klinge, S., Voigts-Hoffmann, F., Leibundgut, M., Arpagaus, S. & Ban, N. Crystal structure of the eukaryotic 60S ribosomal subunit in complex with initiation factor 6. *Science* **334**, 941–948 (2011).
55. Elliff, J. et al. Dynamic states of eIF6 and SDS variants modulate interactions with uL14 of the 60S ribosomal subunit. *Nucleic Acids Res.* **51**, 1803–1822 (2023).
56. Keen, A. N. et al. Eukaryotic initiation factor 6 regulates mechanical responses in endothelial cells. *J. Cell Biol.* **221**, e202005213 (2022).
57. Brina, D., Miluzio, A., Ricciardi, S. & Biffo, S. eIF6 anti-association activity is required for ribosome biogenesis, translational control and tumor progression. *Biochim. Biophys. Acta* **1849**, 830–835 (2015).
58. Jeffery, C. J. Protein moonlighting: what is it, and why is it important? *Philos. Trans. R. Soc. Lond. B. Biol. Sci.* **373**, 20160523 (2018).
59. Mazumder, B. et al. Regulated release of L13a from the 60S ribosomal subunit as a mechanism of transcript-specific translational control. *Cell* **115**, 187–198 (2003).
60. Wan, F. et al. IKKbeta phosphorylation regulates RPS3 nuclear translocation and NF-kappaB function during infection with Escherichia coli strain O157:H7. *Nat. Immunol.* **12**, 335–343 (2011).
61. Kim, T. S., Kim, H. D. & Kim, J. PKCdelta-dependent functional switch of rpS3 between translation and DNA repair. *Biochim Biophys. Acta* **1793**, 395–405 (2009).
62. Ray, P. et al. The Saccharomyces cerevisiae 60 S ribosome biogenesis factor Tif6p is regulated by Hrr25p-mediated phosphorylation. *J. Biol. Chem.* **283**, 9681–9691 (2008).
63. Miluzio, A., Beugnet, A., Volta, V. & Biffo, S. Eukaryotic initiation factor 6 mediates a continuum between 60S ribosome biogenesis and translation. *EMBO Rep.* **10**, 459–465 (2009).

64. Megyesfalvi, Z. et al. Expression patterns and prognostic relevance of subtype-specific transcription factors in surgically resected small-cell lung cancer: an international multicenter study. *J. Pathol.* **257**, 674–686 (2022).
65. Sulzmaier, F. J., Jean, C. & Schlaepfer, D. D. FAK in cancer: mechanistic findings and clinical applications. *Nat. Rev. Cancer* **14**, 598–610 (2014).
66. Aboubakar Nana, F. et al. Increased Expression and activation of FAK in small-cell lung cancer compared to non-small-cell lung cancer. *Cancers* **11**, 1526 (2019).
67. Aboubakar Nana, F. et al. Therapeutic potential of focal adhesion kinase inhibition in small cell lung cancer. *Mol. Cancer Ther.* **18**, 17–27 (2019).
68. Carrano, A. C., Eytan, E., Hershko, A. & Pagano, M. SKP2 is required for ubiquitin-mediated degradation of the CDK inhibitor p27. *Nat. Cell Biol.* **1**, 193–199 (1999).
69. Soria, J. C. et al. A phase I, pharmacokinetic and pharmacodynamic study of GSK2256098, a focal adhesion kinase inhibitor, in patients with advanced solid tumors. *Ann. Oncol.* **27**, 2268–2274 (2016).
70. Zhang, B. et al. Focal Adhesion Kinase (FAK) inhibition synergizes with KRAS G12C inhibitors in treating cancer through the regulation of the FAK-YAP signaling. *Adv. Sci.* **8**, e2100250 (2021).
71. Dawson, J. C., Serrels, A., Stupack, D. G., Schlaepfer, D. D. & Frame, M. C. Targeting FAK in anticancer combination therapies. *Nat. Rev. Cancer* **21**, 313–324 (2021).
72. Calbo, J. et al. A functional role for tumor cell heterogeneity in a mouse model of small cell lung cancer. *Cancer Cell* **19**, 244–256 (2011).
73. Inoue, Y. et al. Extracellular signal-regulated kinase mediates chromatin rewiring and lineage transformation in lung cancer. *Elife* **10**, e66524 (2021).
74. Kinbara, K., Goldfinger, L. E., Hansen, M., Chou, F. L. & Ginsberg, M. H. Ras GTPases: integrins' friends or foes? *Nat. Rev. Mol. Cell Biol.* **4**, 767–776 (2003).
75. Arang, N. et al. High-throughput chemogenetic drug screening reveals PKC-RhoA/PKN as a targetable signaling vulnerability in GNAQ-driven uveal melanoma. *Cell Rep. Med.* **4**, 101244 (2023).
76. Sabari, J. K., Lok, B. H., Laird, J. H., Poirier, J. T. & Rudin, C. M. Unravelling the biology of SCLC: implications for therapy. *Nat. Rev. Clin. Oncol.* **14**, 549–561 (2017).
77. Hu, C. et al. ASCL1 and DLL3 expressions and their clinicopathological implications in surgically resected pure small cell lung cancer: A study of 247 cases from the National Cancer Center of China. *Thorac. Cancer* **13**, 338–345 (2022).
78. Wei, J. et al. Clinicopathological features and prognostic implications of ASCL1 expression in surgically resected small cell lung cancer. *Thorac. Cancer* **12**, 40–47 (2021).
79. Augustyn, A. et al. ASCL1 is a lineage oncogene providing therapeutic targets for high-grade neuroendocrine lung cancers. *Proc. Natl. Acad. Sci. USA* **111**, 14788–14793 (2014).
80. Olsen, R. R. et al. ASCL1 represses a SOX9(+) neural crest stem-like state in small cell lung cancer. *Genes Dev.* **35**, 847–869 (2021).
81. Woods, L. M. et al. Elevated ASCL1 activity creates de novo regulatory elements associated with neuronal differentiation. *BMC Genomics* **23**, 255 (2022).
82. Skoulidis, F. et al. Co-occurring genomic alterations define major subsets of KRAS-mutant lung adenocarcinoma with distinct biology, immune profiles, and therapeutic vulnerabilities. *Cancer Discov.* **5**, 860–877 (2015).
83. Xiao, Z., Zou, Q., Liu, Y. & Yang, X. Genome-wide assessment of differential translations with ribosome profiling data. *Nat. Commun.* **7**, 11194 (2016).
84. Lin, Y. et al. eIF3 Associates with 80S Ribosomes to Promote Translation Elongation, Mitochondrial Homeostasis, and Muscle Health. *Mol. Cell* **79**, 575–587.e577 (2020).
85. Li, F. et al. Reanalysis of ribosome profiling datasets reveals a function of rocaglamide A in perturbing the dynamics of translation elongation via eIF4A. *Nat. Commun.* **14**, 553 (2023).
86. Xiao, Z. et al. De novo annotation and characterization of the translatome with ribosome profiling data. *Nucleic Acids Res.* **46**, e61 (2018).
87. Zhu, Y., Li, F., Yang, X. & Xiao, Z. De novo identification of actively translated open reading frames with ribosome profiling data. *J. Vis. Exp.* https://doi.org/10.3791/63366 (2022).
88. Li, F., Xing, X., Xiao, Z., Xu, G. & Yang, X. RiboMiner: a toolset for mining multi-dimensional features of the translatome with ribosome profiling data. *BMC Bioinforma.* **21**, 340 (2020).
89. Khajuria, R. K. et al. Ribosome levels selectively regulate translation and lineage commitment in human hematopoiesis. *Cell* **173**, 90–103.e119 (2018).
90. Wang, D. et al. Schwann cell-derived EVs facilitate dental pulp regeneration through endogenous stem cell recruitment via SDF-1/CXCR4 axis. *Acta Biomater.* **140**, 610–624 (2022).
91. Killarney, S. T. et al. PKN2 is a dependency of the mesenchymal-like cancer cell state. *Cancer Discov.* **15**, 595–615 (2025).

Acknowledgements

S.S. acknowledges grant support from the National Natural Science Foundation of China (grant no. 82473387) and from the National Clinical Research Center for Geriatrics, West China Hospital, Sichuan University (grant no. Y2022JC002). L. Liu acknowledges financial support ZYGD18021 and ZYJC21002 from the 1.3.5 Project for Disciplines of Excellence, West China Hospital, Sichuan University. M.C. acknowledges grant support from Agence nationale de la recherche of France (grant no. ANR-23-CE14-0023). We thank Li Li, Fei Chen, Chunjuan Bao and Yang Deng from the Institute of Clinical Pathology, West China Hospital of Sichuan University for their technical support with histological staining. We thank Prof. Trudy G Oliver (Duke University, USA) for her generous suggestions for the RPM mouse model.

Author contributions

H.P., Z.W. and M.W. are co-first authors and contributed equally. S.S. and H.P. designed the study. S.S., H.P., L.L., Z.W., M.W. and M.C. interpreted the data and wrote the original draft of the manuscript. H.P., Z.W., M.W., Z. D., K.L., performed RNA-seq and polysome profiling. H.P., Z.W., and M.W. performed ribosome mass spectrometry. H.P., Z.W. and M.W. performed the in vivo experiment. H.P., Z.D., Y.W., M.C., and Y.D. performed bioinformatics analysis. Y.L. performed protein structure analyses. S.S., H.P. and Z.W. performed patient sample multiplex staining and developed an image analysis pipeline. S.Song., X.Y., L.L. and W.W. performed histopathology analysis. Q.P. and L.Liu. provided administrative support and data resources, collected patient samples. S.S. supervised the overall study, provided strategic oversight and conceived the study.

Competing interests

The authors declare the following competing interests: S. Shen reports personal fees from Agence nationale de la recherche (France), Krebsliga Schweiz (Switzerland), KWF Kankerbestrijding (Netherlands), Austrian Research Funding, Belgian Foundation against Cancer, Shenzhen Medical Academy of Research and Translation (China), and serving as an Associate Editor for Oncogenesis (Springer Nature, London, UK); M. Cerezo is a CSO for BiPer Therapeutics (Strasbourg, France) and reports personal fees from European Commission. The remaining authors declare no competing interests.

Additional information

Supplementary information The online version contains supplementary material available at https://doi.org/10.1038/s41467-026-69899-8.

Correspondence and requests for materials should be addressed to Lunxu Liu or Shensi Shen.

Peer review information *Nature Communications* thanks Pierre Close, Oskar Marin-Bejar and the other anonymous reviewer(s) for their contribution to the peer review of this work. A peer review file is available.